

Unfolding the geometric structure and multiple timescales of the urea–urease pH oscillator

Arthur V. Straube,^{1,2} Guillermo Olicón Méndez,³ Stefanie Winkelmann,¹ Felix Höfling,^{2,1} and Maximilian Engel^{2,4}

¹⁾*Zuse Institute Berlin, Takustraße 7, 14195 Berlin, Germany*

²⁾*Freie Universität Berlin, Department of Mathematics and Computer Science, Arnimallee 6, 14195 Berlin, Germany^{a)}*

³⁾*Universität Potsdam, Institut für Mathematik, Karl-Liebknecht-Straße 24, 14476 Potsdam, Germany.*

⁴⁾*KdVI Institute for Mathematics, University of Amsterdam, The Netherlands*

We study a two-variable dynamical system modeling pH oscillations in the urea–urease reaction within giant lipid vesicles — a problem that intrinsically contains multiple, well-separated timescales. Building on an existing, deterministic formulation via ordinary differential equations, we resolve different orders of magnitude within a small parameter and analyze the system’s limit cycle behavior using geometric singular perturbation theory (GSPT). By introducing two different coordinate scalings — each valid in a distinct region of the phase space — we resolve the local dynamics near critical fold points, using the extension of GSPT through such singular points due to Krupa and Szmolyan. This framework enables a geometric decomposition of the periodic orbits into slow and fast segments and yields closed-form estimates for the period of oscillation. In particular, we link the existence of such oscillations to an underlying biochemical asymmetry, namely, the differential transport across the vesicle membrane.

Keywords: Fast-slow system, geometric singular perturbation theory, relaxation oscillations, biochemical oscillators, clock reactions

^{a)}Electronic mail: straube@zib.de

I. INTRODUCTION

Oscillatory rhythms are ubiquitous in biophysical systems, underpinning essential functions such as spatiotemporal self-organization, cellular signaling, metabolism, and homeostasis.^{1–7} These dynamics are often mediated by enzymes, which play a central role in intracellular kinetics and typically operate on multiple timescales, embedded in complex feedback mechanisms that regulate their activity.^{8–13} Enzymatic activity and cellular function are highly sensitive to environmental factors, in particular to the level of acidity or pH.^{6,10,14–16} Systems exhibiting periodic changes in pH are known as *pH oscillators*.^{17–21} While many studies of such oscillators have focused on closed reactors, recent work has increasingly turned to open reaction compartments that exchange matter with their surroundings,^{22–29} enabling the sustained operation of chemical switches or clocks.^{30–32} In this work, we analyze the urea–urease reaction confined to a lipid vesicle—a minimal model system in which urease catalyzes the hydrolysis of urea in a pH-dependent manner, while the vesicle membrane permits exchange of acid and substrate with the surrounding medium. This biologically and technologically relevant setting^{33–37} gives rise to fast–slow oscillatory dynamics that can be captured by low-dimensional models.^{38,39} Controlling the timescale separation, we uncover the geometric structure underlying the resulting limit cycle dynamics using methods from geometric singular perturbation theory (GSPT)^{40,41} which has proven to be a powerful mathematical tool in the context of (bio)chemical reactions.^{42–45}

The model. We study the two-variable ODE model derived in Ref. 39, which deterministically describes pH oscillations in the urea–urease reaction confined to a giant lipid vesicle. Further reduction of this model (Appendix A) leads to the following dynamical system in the dimensionless variables $s \geq 0$ and $h \geq 0$, representing rescaled concentrations of the substrate molecules S and hydrogen ions H^+ , respectively:

$$\frac{ds}{dt} = f(s, h) := -r(h)s + K_s, \quad (1a)$$

$$\frac{dh}{dt} = g(s, h) := -q(s, h) + K_h(1 - h), \quad (1b)$$

where $K_s, K_h > 0$ are positive constants. The rate function $r(h)$, which determines the consumption of the substrate s , has the form

$$r(h) = \left(\beta \varepsilon_1 / h + 1 + \beta h / \varepsilon_1 \right)^{-1} > 0, \quad (2)$$

with a small parameter $\varepsilon_1 > 0$ and some constant $\beta > 0$. This function exhibits a single maximum and tends to zero as $h \rightarrow \infty$ or $h \rightarrow 0$. The consumption of hydrogen $h \geq 0$ is governed by the reaction speed $q(s, h)$, which is given as the non-negative root of the quadratic equation $q^2 + v(h)q - K\varepsilon_2^{-1}r(h)h^2s = 0$:

$$q(s, h) = -\frac{1}{2}v(h) + \frac{1}{2}\sqrt{v(h)^2 + 4K\varepsilon_2^{-1}r(h)h^2s} \geq 0, \quad (3)$$

where $v(h)$ is defined as

$$v(h) := \alpha K\varepsilon_2^{-1}h^2 - K_h(1 - h), \quad (4)$$

with constants $\varepsilon_2, \alpha, K, K_h > 0$. We note that for fixed s , the function $q(s, h)$ vanishes as $h \rightarrow \infty$, while as $h \rightarrow 0$ it asymptotically behaves like $-v(h)$. Second, ε_1 appears only in the combination h/ε_1 and ε_2 only in h^2/ε_2 ; this observation has been motivating for the approach followed below. An exemplary numerical solution of the ODE system (1) is plotted in Fig. 1(a).

Biochemical background and interpretation. System (1) models the urease-assisted catalysis of urea, serving as the substrate S , with the reaction rate depending on the hydrogen ion (or proton) concentration, i.e., on the pH value quantifying the acidity. Urease, an enzyme acting as a biological catalyst, regulates the speed of the catalytic reaction via the term $r(h)s$, where $r(h)$ is the hydrogen-dependent reaction rate. The effective decay of hydrogen^{38,39} is governed by the function $q(s, h)$, which captures the nonlinear coupling between substrate and proton concentrations.

The described process occurs in an open reactor – a unilamellar vesicle enclosed by a membrane partially permeable to chemical species. Exchange with the surrounding medium ensures a continuous supply of both substrate and acid, with influx rate constants K_s and K_h , respectively. Inside the vesicle, the core reaction acts as a chemical switch or clock,^{30–32} rapidly driving the system from acidic to basic conditions. In turn, the external inflow of acid and substrate resets the pH clock after each cycle, enabling sustained oscillations. These oscillations result from the interplay between internal switching dynamics and external replenishment, and are characterized by fast–slow transitions between acidic and basic phases. A detailed derivation of the simplified, dimensionless system (1) from a previously reduced model of the urea–urease reaction network³⁹ is presented in Appendix A.

Previous studies have shown that the system under consideration—like those in Refs. 38, 39—captures a practically relevant and experimentally realistic setting; for further insights,

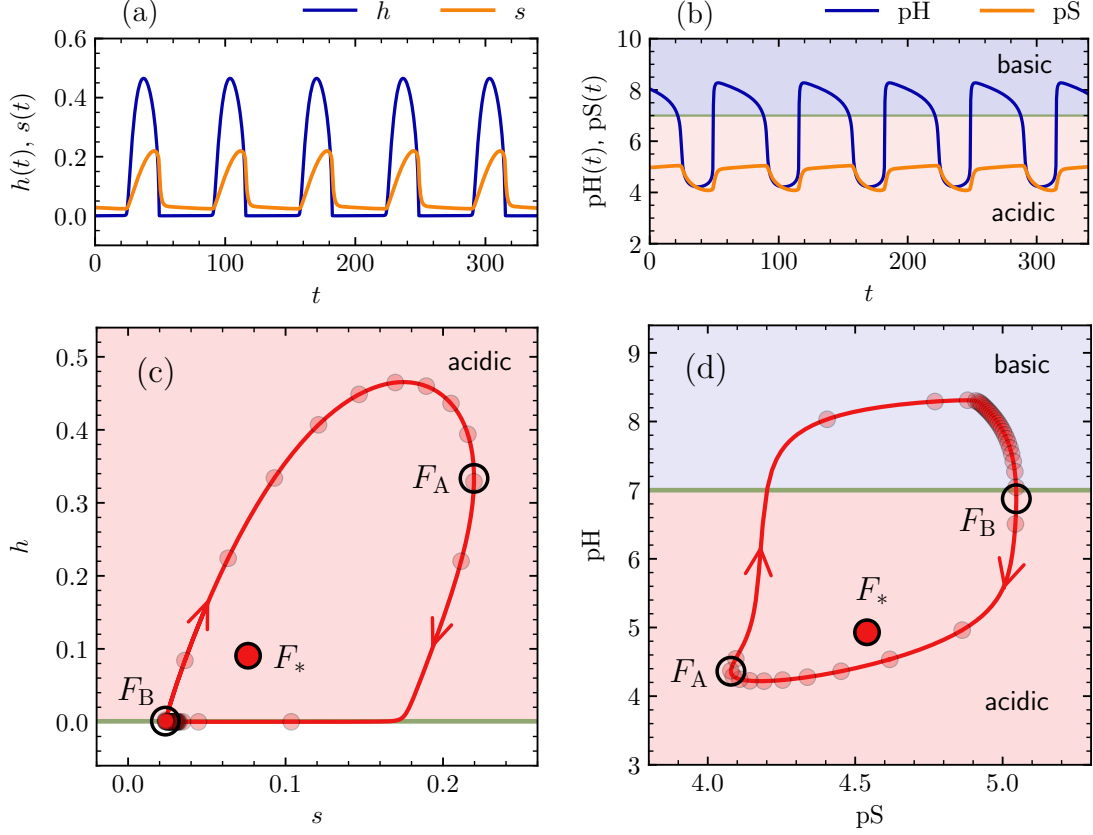


FIG. 1. Panels (a) and (b) show a typical numerical solution of Eq. (1) for the parameter values listed in Table III; panels (c) and (d) depict the corresponding limit cycles for the same data (red solid lines). Left panels [(a) and (c)] use the original (s, h) variables, while right panels [(b) and (d)] employ the negative logarithms (pS, pH) , commonly used in chemistry,^{25,39} see Eq. (A9). In the bottom panels, arrows indicate the direction of motion, and disks show the evolution of the variables sampled equidistantly in time. The limit cycle encloses the only fixed point (dark red disc in panels (c) and (d)), which is repelling and located at $F_* = (s_*, h_*) \approx (0.0762, 0.0906)$ and $(\text{pS}_*, \text{pH}_*) \approx (4.54, 4.93)$, respectively. The turning points F_A and F_B mark those points on the limit cycle with the largest and smallest values of s and the smallest and largest values of pS , respectively. Note that smaller values of pS and pH correspond to larger values of s and h and vice versa, which effectively flips the direction of the axes and changes the relative location of points F_A and F_B . The horizontal green line represents the neutral value, $\text{pH} = 7$ ($h = h_{\max}$, see Section II.1), separating acidic ($\text{pH} < 7$, $h > h_{\max}$, shaded light red) and basic ($\text{pH} > 7$, $h < h_{\max}$, shaded light blue in panels (b) and (d)) domains.

see Ref. 46. One of the strengths of our study is to build on this foundation and rigorously analyze the model’s complex oscillatory behavior. However, due to this realism and unlike many mathematically idealized systems, the present model does not feature a single small parameter that would directly justify a standard fast–slow decomposition or suggest an obvious timescale separation. For parameter regimes relevant to experiments, numerical integration of system (1) reveals stable limit cycle solutions, characterized by very different time scales along the segments of the cycle (Fig. 1). This timescale separation manifests itself in the form of mixed-mode oscillations, which fall outside the direct applicability of classical singular perturbation theory. In particular, the dynamics is governed by multiple small dimensionless parameter combinations, none of which alone controls the system’s behavior.

To address this obstacle to analysis via GSPT,^{40,41} we identify a suitable formalization of the timescale separation that emerges from the interplay of multiple small parameters. This enables the application of GSPT, combining the conventional Fenichel’s theory for normally hyperbolic critical manifolds⁴⁷ with its extension to nonhyperbolic points, such as folds and canards, developed via blow-up techniques.⁴⁸ Using this framework, we characterize the structure of the limit cycle and quantify its decomposition into alternating fast and slow segments. Two key components of the limit cycle are stable branches of distinct critical manifolds—one under acidic pH conditions, the other under basic pH conditions—each requiring a different rescaling to resolve the local dynamics. We complete the global picture of the oscillation mechanism by constructing transition maps between suitable Poincaré sections.

In Section II, we present initial observations, establish the existence of a limit cycle, and introduce a rescaling in terms of a single small parameter. The existence of a limit cycle was conjectured in earlier work,³⁹ based on the presence of a single repelling fixed point and an application of the Poincaré–Hopf index theory. Here, we provide a more rigorous proof using the Poincaré–Bendixson theorem. Section III contains the core of our analysis: we apply GSPT to resolve the dynamics near the fold points at low and neutral pH (Section III.1 and Section III.2), construct the global structure of the limit cycle and compare with numerical solutions (Section III.3). We discuss the implications for the chemical system at hand (Section IV) and conclude in Section V.

II. INITIAL OBSERVATIONS AND ANALYTICAL SETUP

In this section, we briefly discuss a parameter regime where Eq. (1) exhibits oscillatory solutions and we give a necessary conditions for the existence of a limit cycle. We suggest a coupling of the small parameters ε_1 and ε_2 to proceed with a single small parameter ε , which allows converting system (1) into a fast-slow system in standard form.

II.1. Observation of sustained oscillations

Figure 1 shows a typical limit cycle solution of system (1), using the variables (s, h) and, alternatively, their negative logarithms, (pS, pH) , employed in biochemistry (see Eq. (A9) for the conversion relation). From the representations in Fig. 1, one anticipates the presence of multiple timescales: in panels (a) and (b), kinks and rapid variations in time and, in panels (c) and (d), an uneven spacing of markers placed equidistantly in time along the solution, especially in the vicinity of point F_B . The chosen parameter values are listed in Table III in Appendix A and are the same as in a previous study,³⁹ approximately resembling the experimental situation: while β is fixed by the properties of the urease enzyme and K_s and K_h are given by the specific permeabilities of the vesicle membrane, α , ε_1 , and ε_2 can be controlled through the external concentrations of substrate and hydrogen ion, outside of the vesicle.

The position h_{\max} of the maximum of the consumption rate $r(h)$ (see Eq. (2)) is determined by $r'(h_{\max}) = 0$, yielding $h_{\max} = \varepsilon_1$. For the given parameters, it corresponds to the neutral value of $\text{pH} = 7$ (green horizontal lines in Figs. 1(b), 1(d)). At $h = h_{\max}$, the conversion of substrate into product is most efficient and any deviation from the optimal level of pH slows down the corresponding reaction rate $r(h)$. The limit cycle crosses this line and one part of it belongs to the acidic domain (shaded light red) with $\text{pH} < 7$ ($h > h_{\max}$) and part to the basic domain (shaded light blue), where $\text{pH} > 7$ ($h < h_{\max}$). Using linear scales for the variables s and h , as in Fig. 1(a) and (c), the basic region is not well resolved: the neutral value, $\text{pH} = 7$, corresponds to $h = h_{\max} \approx 7.7 \times 10^{-4}$, being compressed and pushed against the $h = 0$ axis. Accordingly, the turning point F_A lies deeply in the acidic domain, while the turning point F_B is located in the vicinity of the neutral pH . As we will show below, the position of the turning point F_B , which underlies the geometric structure

of the limit cycle, is determined exactly by the maximum of the function $r(h)$.

II.2. Existence of the limit cycle

Generally, the system under consideration, Eq. (1), exhibits either a steady-state solution or oscillations at long times. Focusing on the limit cycle, we briefly outline the region of parameters where sustained oscillations take place.

The s - and h -nullclines of system (1), denoted as \mathcal{N}_s and \mathcal{N}_h , respectively, are parametrized as

$$\mathcal{N}_s = \{(n_s(h), h) : h \geq 0\}, \quad n_s(h) := \frac{K_s}{r(h)}, \quad (5a)$$

and

$$\mathcal{N}_h = \{(n_h(h), h) : h \geq 0\}, \quad n_h(h) := \frac{\alpha K_h(1-h)}{r(h)}. \quad (5b)$$

The unique equilibrium $F_* = (s_*, h_*) \in \mathbb{R}_{>0}^2$ solves $n_h(h_*) = n_s(h_*) =: s_*$ for

$$s_* = \frac{K_s}{r(h_*)} > 0, \quad h_* = 1 - \frac{K_s}{\alpha K_h} > 0. \quad (6)$$

For the parameter values in Table III, used to generate data in Fig. 1, we obtain $F_* = (s_*, h_*) \approx (0.0762, 0.0906)$ or $(\text{pS}_*, \text{pH}_*) \approx (4.54, 4.93)$.

Remark 1. In the following, we require that $\alpha K_h > K_s$, so that F_* exists in the positive quadrant, in particular, the concentration h_* is positive. We note that this condition on the parameters aligns with a general claim made in a previous study for the existence of a limit cycle—namely, differential transport of substrate and hydrogen across the membrane,³⁸ which will be discussed further in Section V. The ratio K_h/K_s quantifies the difference in the transport of the hydrogen ions and substrate across the membrane, and $(2\alpha)^{-1} = [\text{S}_{\text{ext}}]/[\text{H}_{\text{ext}}^+]$ represents the ratio of their external concentrations, see Appendix A.

The stability of the equilibrium point is determined by the Jacobian matrix of Eq. (1) at F_* , which we denote as $J = \partial(f, g)/\partial(s, h)|_{F_*}$. The trace $\text{Tr } J$ exhibits a sign change, suggesting that the system admits a *Hopf bifurcation*.⁴⁹ Figure 2 depicts the numerically determined domain of oscillations in the parameter plane $(K_h/K_s, 1/\alpha)$; outside this domain, the orbits of the system converge to the unique steady state, provided $\alpha K_h > K_s$.

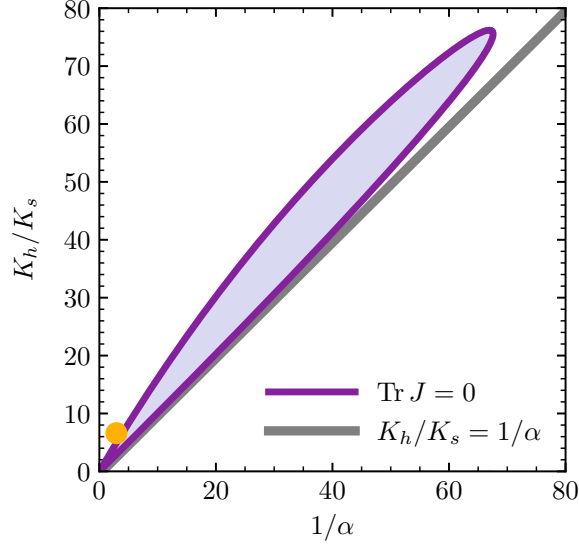


FIG. 2. Numerical results for the domain of oscillation in the parameter combinations $(K_h/K_s, \alpha^{-1})$ at fixed values of β , ε_1 , and ε_2 (Table III). The curve $\text{Tr } J = 0$ (violet line) separates the regions of stable (attractive) and unstable (repelling) behavior of the fixed point. Oscillations occur in the blue-shaded region, where the fixed point is a repelling node or focus, $\text{Tr } J > 0$. The yellow disc marks the parameter values of the real-world system^{38,39} (see Tables II and III), for which the limit cycle is shown in Fig. 1. A lower bound for oscillations is given by the straight line, $K_h/K_s = \alpha^{-1}$, see Eq. (6).

The domain of oscillations in the parameter space is bounded from below by the condition $K_h/K_s = \alpha^{-1}$.

By means of standard phase-plane analysis, the existence of an attracting limit cycle of (1) is guaranteed as long as the equilibrium F_* is unstable, as stated in the following proposition:

Proposition 1. Consider system (1) with $\alpha K_h > K_s$ such that F_* given by Eq. (6) is the equilibrium. If the parameter values are such that $\text{Tr } J|_{F_*}$ and $\text{Det } J|_{F_*}$ are positive, then system (1) admits an attracting limit cycle contained in the positive quadrant $\mathbb{R}_{\geq 0}^2 := \{(s, h) : s, h \geq 0\}$.

Proof. We construct a positively invariant compact region \mathcal{R} contained in $\mathbb{R}_{> 0}^2$. First, let us fix any $h_{\text{top}} > 1$, an arbitrarily large $s_{\text{nul}} > \max\{K_s/r(h_{\text{top}}), s_*\}$, and the point $(s_{\text{nul}}, h_{\text{nul}}) \in \mathcal{N}_s$. Choose the unique initial condition $(0, h_0)$ such that its forward semiorbit

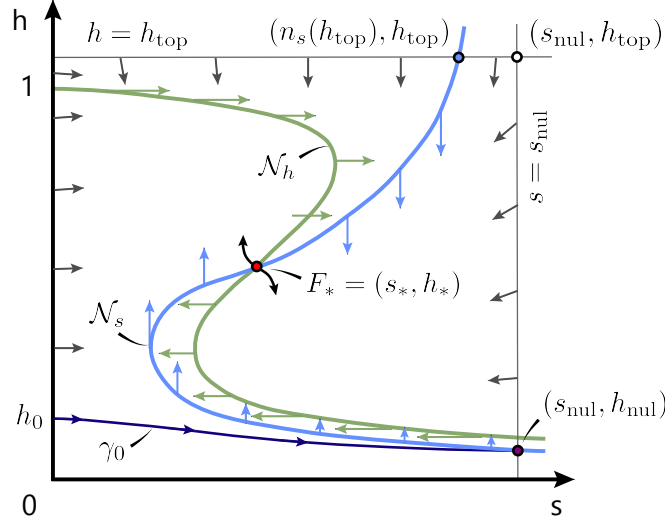


FIG. 3. A schematic supporting the proof of Prop. 1. The s - and h -nullclines, \mathcal{N}_s and \mathcal{N}_h , are shown as light blue and green lines, respectively; arrows indicate the direction of the flow field at the corresponding nullclines. The top, $h = h_{\text{top}}$, and right, $s = s_{\text{nul}}$, border of the compact region are given by the horizontal and vertical straight lines, respectively. The bottom border is given by the semiorbit γ_0 starting at $(0, h_0)$ and ending at $(s_{\text{nul}}, h_{\text{nul}})$ and is plotted in dark blue. Other characteristic intersection points, including the fixed point $F_* = (s_*, h_*)$, are shown as colored circle markers.

$\gamma_0 := \{(s(t), h(t)) : t \geq 0, (s(0), h(0)) = (0, h_0)\}$ intersects \mathcal{N}_s at $(s_{\text{nul}}, h_{\text{nul}})$. Consider the compact region $\mathcal{R} \subset \mathbb{R}_{\geq 0}^2$ delimited by γ_0 , $\{s = s_{\text{nul}}\}$, $\{h = h_{\text{top}}\}$, and $\{s = 0\}$, which is positively invariant for sufficiently large s_{nul} , see Fig. 3. Indeed, the vector field given by Eq. (1) points inwards on $\partial\mathcal{R}$, apart from γ_0 on which it is tangent. This follows from the fact that

$$\begin{aligned} \dot{s} &> 0, \text{ when } s = 0, \\ \dot{s} &< 0, \text{ when } s = s_{\text{nul}} \text{ as } s_{\text{nul}} > \frac{K_s}{r(h)}, \text{ for all } h \in [h_{\text{nul}}, h_{\text{top}}], \\ \dot{h} &\leq K_h(1 - h) < 0 \text{ when } h = h_{\text{top}} > 1. \end{aligned}$$

Since F_* is an unstable node or focus, as indicated by $\text{Tr } J|_{F_*} > 0$ and $\text{Det } J|_{F_*} > 0$, the result follows from the Poincaré–Bendixson theorem (cf. e.g. Ref. 50 [Chapter 16, Theorem 2.1]). \square

II.3. Introduction of a single small parameter

We have seen that, for a suitable choice of parameter values, system (1) admits an attracting limit cycle, which displays slow and fast regimes. We will demonstrate below that the time scale separation emerges in a suitable limit process for the small parameters ε_1 and ε_2 . One observes that ε_1^2 and ε_2 are of similar order of magnitude (see Table III, and by the only occurrence of ε_1 and ε_2 through the combinations h/ε_1 and h^2/ε_2 in the model, Eqs. (2)–(4). This structure suggests to use a scaling $\varepsilon_1 = \mathcal{O}(\varepsilon)$ and $\varepsilon_2 = \mathcal{O}(\varepsilon^2)$ as $\varepsilon \rightarrow 0$ such that h/ε_1 and h^2/ε_2 can remain balanced if $h = \mathcal{O}(\varepsilon)$. Concretely, we set

$$\varepsilon_1 =: C\varepsilon \quad \text{and} \quad \varepsilon_2 =: A^{-1}\varepsilon^2, \quad (7)$$

with the constant $C \approx 0.77$ chosen for convenience such that $\varepsilon = 10^{-3}$ for the parameters of the real-world system in Table III; it follows that $A \approx 1.4$. Upon substituting in Eq. (1), the system reads

$$\frac{ds}{dt} = -r_\varepsilon(h)s + K_s, \quad (8a)$$

$$\frac{dh}{dt} = -q_\varepsilon(s, h) + K_h(1 - h), \quad (8b)$$

with the functions

$$r_\varepsilon(h) := \frac{1}{\beta C(h/\varepsilon)^{-1} + 1 + \beta C^{-1}(h/\varepsilon)}, \quad (9a)$$

$$q_\varepsilon(s, h) := \frac{1}{2}\sqrt{v_\varepsilon(h)^2 + 4AKr_\varepsilon(h)(h/\varepsilon)^2s} - \frac{1}{2}v_\varepsilon(h), \quad (9b)$$

where $v_\varepsilon(h)$ is the quadratic function

$$v_\varepsilon(h) := \alpha AK(h/\varepsilon)^2 - K_h(1 - h), \quad (10)$$

as induced by $v(h)$ defined in Eq. (4). The equilibrium of Eq. (8) is calculated analogously to Eq. (6) and is located at $F_{*,\varepsilon} := (s_{*,\varepsilon}, h_{*,\varepsilon}) = (K_s/r_\varepsilon(h_*), h_*)$; in particular, $h_{*,\varepsilon} = h_*$ is independent of ε , but $s_{*,\varepsilon} = \mathcal{O}(\varepsilon^{-1})$ diverges as $\varepsilon \rightarrow 0$.

III. FAST-SLOW ANALYSIS OF THE SYSTEM

For the fast-slow analysis of the pH oscillator, described by the dynamical system (8), we employ GSPT techniques^{40,41} to obtain and characterize the critical manifold, which

pertains to the singular limit ($\varepsilon = 0$) and reveals the geometric structure underlying the limit cycle for ε small enough. Figure 1 illustrates the limit cycle for the original system, which, after rescaling of constants, corresponds to $\varepsilon = 10^{-3}$; decreasing ε further enhances the timescale separation. Numerical integration of Eq. (8) shows that, while the limit cycle deforms, it remains bounded in the h -variable, but progressively extends in the s -variable. However, when represented in terms of the rescaled variable $\sigma = \varepsilon s$, see Fig. 4(a), the limit cycle becomes bounded and appears to converge to a specific shape as ε is decreased. This observation motivates us, in Section III.1, to perform the fast-slow analysis in the variables (σ, h) . It reveals the slow and fast motions in the acidic domain ($h > h_{\max}$), including the fold point F_A , but it cannot resolve the fold point F_B approached from the basic domain ($h < h_{\max}$), which is close to the $h = 0$ line. We address this issue in Section III.2 by introducing another rescaling, (s, η) with $\eta = h/\varepsilon$, which can capture the dynamics near F_B , but not in the acidic regime.

The two rescalings provide different perspectives on the limit cycle, corresponding to two charts K_A and K_B , which overlap and can be matched, as depicted in Fig. 4. In both charts, we first focus on the singular limit $\varepsilon = 0$ and identify the critical manifolds, which are *normally hyperbolic* away from the points F_A and F_B . These invariant manifolds persist as invariant slow manifolds for ε small enough, and can be extended beyond the generic fold points F_A and F_B using techniques of GSPT generalized for degenerate equilibria.^{40,48} It implies that a trajectory moving rightwards along the slow manifold in chart K_A (thick black solid line in Fig. 4(b)) passes the fold point F_A and transitions to a fast fiber pointing downwards (vertical solid gray line). Similarly, in chart K_B , a trajectory moving leftwards along the slow manifold passes the fold point F_B and quickly moves vertically upwards, see Fig. 4(c). A coordinate transformation matches the dynamics in charts K_A and K_B , as discussed in Section III.3, ultimately resolving the mixed-mode dynamics of the limit cycle.

III.1. The fold point F_A approached from the acidic domain, at low pH

For investigating the turning point F_A located in the acidic domain, at relatively large values of h (low pH level), we use the rescaled variables

$$\sigma = \varepsilon s, \quad \tau := \varepsilon t, \quad (11)$$

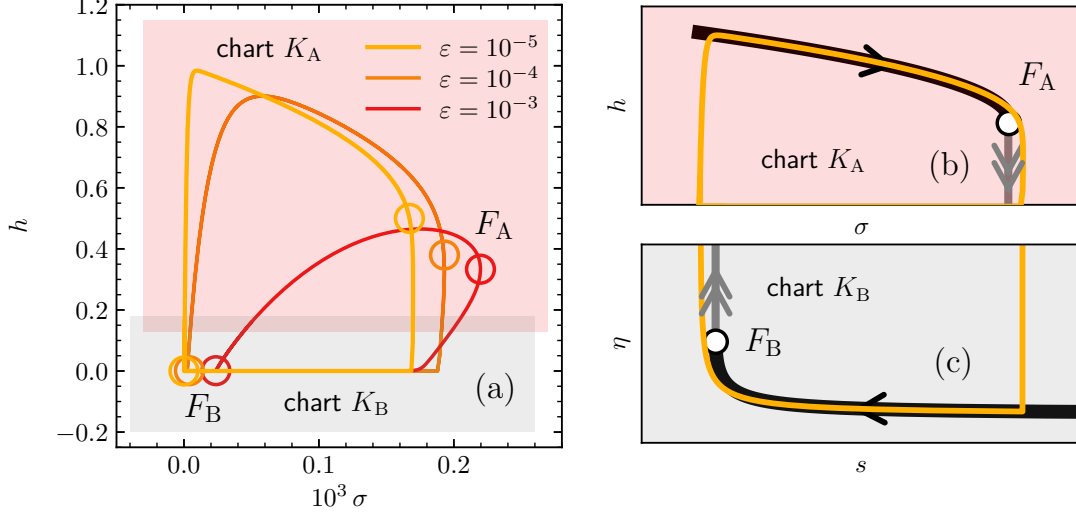


FIG. 4. (a): Numerical solutions of Eq. (8) for $\varepsilon = 10^{-5}, 10^{-4}, 10^{-3}$ showing the limit cycle trajectories and their fold points in the variables (σ, h) with $\sigma = \varepsilon s$. Shaded regions depict the mutual arrangement of the charts K_A and K_B associated with the two rescalings, as described in the text. (b) and (c): Charts K_A in the variables (σ, h) and K_B in the variables (s, η) , showing the transition from their slow manifolds (solid black lines) to fast fibers (solid gray lines) at the fold points F_A and F_B (open circles) for $\varepsilon = 0$, respectively; the variables are connected through $\sigma = \varepsilon s$ and $h = \varepsilon \eta$. The yellow solid line is an ε -perturbed trajectory ($\varepsilon = 10^{-5}$), which illustrates how switching between the charts leads to a closed orbit.

where σ is a small variable and τ is a slow time relative to the original variables s and t , respectively. With this ansatz, the dynamical system (8) becomes the fast-slow system

$$\frac{d\sigma}{d\tau} = \tilde{f}_\varepsilon(\sigma, h) := -\tilde{r}_\varepsilon(h)\sigma + K_s, \quad (12a)$$

$$\varepsilon \frac{dh}{d\tau} = \tilde{g}_\varepsilon(\sigma, h) := -\tilde{q}_\varepsilon(\sigma, h) + K_h(1 - h), \quad (12b)$$

with $\tilde{r}_\varepsilon(h) := \varepsilon^{-1}r_\varepsilon(h)$ and $\tilde{q}_\varepsilon(\sigma, h) := q_\varepsilon(\sigma/\varepsilon, h)$. Inserting the definitions of r_ε and q_ε from Eqs. (9a) and (9b), we obtain

$$\tilde{r}_\varepsilon(h) = \frac{1}{\varepsilon^2 \beta C / h + \varepsilon + (\beta / C)h} \quad (13)$$

and

$$\tilde{q}_\varepsilon(\sigma, h) = -\frac{1}{2\varepsilon^2} \left[\sqrt{\tilde{v}_\varepsilon(h)^2 + 4\varepsilon^2 AK \tilde{r}_\varepsilon(h) h^2 \sigma} - \tilde{v}_\varepsilon(h) \right], \quad (14)$$

where

$$\tilde{v}_\varepsilon(h) := \varepsilon^2 v_\varepsilon(h) = \alpha AK h^2 - \varepsilon^2 K_h (1 - h) \quad (15)$$

for $v_\varepsilon(h)$ given in Eq. (10). Switching back to the timescale t , we rewrite the fast-slow system (12) as

$$\frac{d\sigma}{dt} = \varepsilon \tilde{f}_\varepsilon(\sigma, h), \quad (16a)$$

$$\frac{dh}{dt} = \tilde{g}_\varepsilon(\sigma, h). \quad (16b)$$

III.1.1. Critical manifold and singular dynamics

The *layer problem* describes the fast, one-dimensional dynamics of $h > 0$ for fixed σ , which acts as a parameter. It is obtained from the fast system Eq. (16) by setting $\varepsilon = 0$:

$$\frac{d\sigma}{dt} = 0, \quad (17a)$$

$$\frac{dh}{dt} = \tilde{g}_0(\sigma, h). \quad (17b)$$

However, $\tilde{g}_0(\sigma, h)$ is initially undefined, as $\tilde{g}_\varepsilon(\sigma, h)$ becomes singular at $\varepsilon = 0$, see Eq. (14). A continuous extension $\tilde{q}_0(\sigma, h) := \lim_{\varepsilon \rightarrow 0} \tilde{q}_\varepsilon(\sigma, h)$ is obtained by distinguishing the sign of $v_\varepsilon(h)$, which allows us to rewrite $\tilde{q}_\varepsilon(\sigma, h)$ as

$$\tilde{q}_\varepsilon(\sigma, h) = \begin{cases} -\frac{\tilde{v}_\varepsilon(h)}{2\varepsilon^2} \left[1 + \sqrt{1 + \varepsilon^2 4AK\tilde{r}_\varepsilon(h)h^2\sigma/\tilde{v}_\varepsilon(h)^2} \right], & \text{if } 0 < h < h_\varepsilon^+, \\ \varepsilon^{-1} \sqrt{AK\tilde{r}_\varepsilon(h)h^2\sigma}, & \text{if } h = h_\varepsilon^+, \\ \frac{2AK\tilde{r}_\varepsilon(h)h^2\sigma}{\tilde{v}_\varepsilon(h)} \left[1 + \sqrt{1 + \varepsilon^2 4AK\tilde{r}_\varepsilon(h)h^2\sigma/\tilde{v}_\varepsilon(h)^2} \right]^{-1}, & \text{if } h > h_\varepsilon^+, \end{cases} \quad (18)$$

in terms of the positive root h_ε^+ of the equation $v_\varepsilon(h) = 0$:

$$h_\varepsilon^+ = \varepsilon \frac{-\varepsilon K_h + \sqrt{(\varepsilon K_h)^2 + 4\alpha AK K_h}}{2\alpha AK}. \quad (19)$$

Thus, $h_\varepsilon^+ \rightarrow 0$ as $\varepsilon \rightarrow 0$, and for all $h > 0$ the following holds:

$$\tilde{q}_0(\sigma, h) = \frac{AK\tilde{r}_0(h)h^2\sigma}{\tilde{v}_0(h)} = \frac{C\sigma}{\alpha\beta h}, \quad (20)$$

upon inserting $\tilde{r}_0(h) = C/(\beta h)$ and $\tilde{v}_0(h) = \alpha AK h^2$, see Eqs. (13) and (15).

The so-called *reduced problem* is obtained from Eq. (12) by setting $\varepsilon = 0$; it has the form of a differential-algebraic equation:

$$\frac{d\sigma}{d\tau} = \tilde{f}_0(\sigma, h) := -\frac{C\sigma}{\beta h} + K_s, \quad (21a)$$

$$0 = \tilde{g}_0(\sigma, h) := -\frac{C\sigma}{\alpha\beta h} + K_h(1 - h). \quad (21b)$$

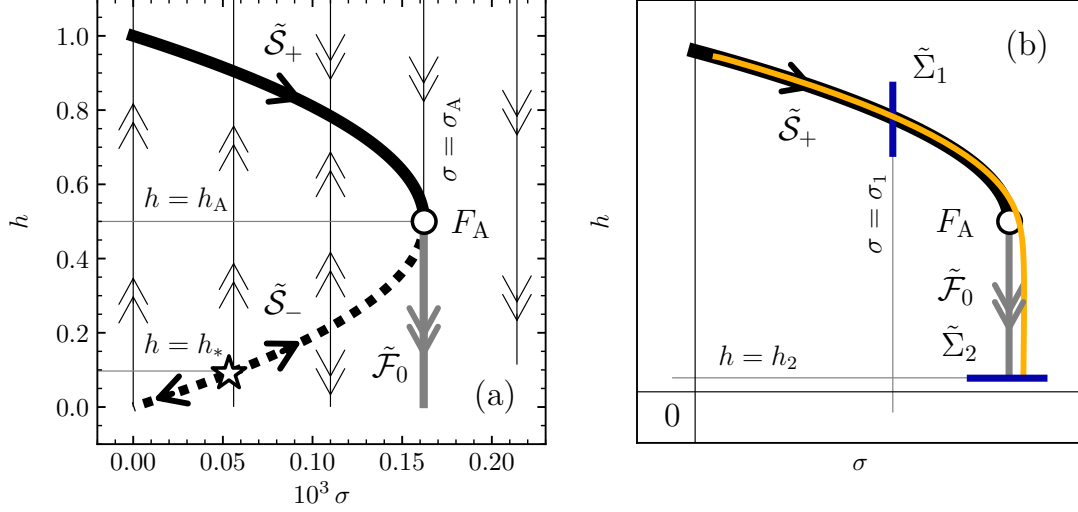


FIG. 5. (a) The critical manifold $\tilde{\mathcal{S}}_A = \tilde{\mathcal{S}}_+ \cup \{F_A\} \cup \tilde{\mathcal{S}}_-$ (thick black lines) consists of the fold point F_A (open circle, Eq. (23)), the attractive branch $\tilde{\mathcal{S}}_+$ (solid line) and the repelling branch $\tilde{\mathcal{S}}_-$ (dotted line), see Eq. (22). The slow motion along $\tilde{\mathcal{S}}_+$ is governed by Eq. (26) and progresses towards the generic fold point F_A , where a loss of hyperbolicity triggers a transition to fast motion along the fast fiber. The segment of the fast fiber extending downward from F_A , denoted as $\tilde{\mathcal{F}}_0$ (thick gray line), is given by Eq. (17b) for $\sigma = \sigma_A$. The thin horizontal gray lines indicate $h = h_A$ and $h = h_*$; the star indicates the fixed point of system (21). (b) Schematic of the ε -perturbed extension (solid yellow line) of the critical manifold from panel (a), following $\tilde{\mathcal{S}}_{+, \varepsilon}$ and passing near the fold point F_A . The Poincaré sections $\tilde{\Sigma}_1$ and $\tilde{\Sigma}_2$ are shown as dark blue lines. The thin gray lines are for $\sigma = \sigma_1$ and $h = h_2$, respectively; the remaining symbols are as in (a).

The *critical manifold* consists of the equilibria of the layer problem, Eq. (17b), and is determined by the zeros of \tilde{g}_0 , given by

$$\tilde{\mathcal{S}}_A = \left\{ (\varphi(h), h) : h > 0 \right\} \quad \text{with} \quad \varphi(h) := \frac{\alpha\beta K_h}{C} h(1-h). \quad (22)$$

The function $\varphi(h)$ possesses only one extremum at $h = 1/2$, which corresponds to the acidic fold point

$$F_A := (\sigma_A, h_A) = (\varphi(h_A), h_A) = \left(\frac{\alpha\beta K_h}{4C}, \frac{1}{2} \right). \quad (23)$$

The stability of the manifold $\tilde{\mathcal{S}}_A$ is determined by the sign of the derivative $\partial_h \tilde{g}_0(\sigma, h)$ on

$\tilde{\mathcal{S}}_A$:

$$\begin{aligned} \partial_h \tilde{g}_0(\sigma, h) \Big|_{(\sigma, h) \in \tilde{\mathcal{S}}_A} &= \partial_h \left(-\frac{C\sigma}{\alpha\beta h} + K_h(1-h) \right) \Big|_{(\sigma, h) \in \tilde{\mathcal{S}}_A} \\ &= -2K_h \frac{h - h_A}{h}. \end{aligned} \quad (24)$$

In particular, $\partial_h \tilde{g}_0$ changes sign at F_A . The critical manifold $\tilde{\mathcal{S}}_A$ contains the sets $\tilde{\mathcal{S}}_+$ and $\tilde{\mathcal{S}}_-$, where $\tilde{\mathcal{S}}_+$ represents the attractive upper branch for $h > h_A$, characterized by $\partial_h \tilde{g}_0(\sigma, h) < 0$, and $\tilde{\mathcal{S}}_-$ represents the repelling lower branch for $h < h_A$, characterized by $\partial_h \tilde{g}_0(\sigma, h) > 0$, see Fig. 5(a). The manifold is therefore normally hyperbolic everywhere except at the fold point F_A .

The slow dynamics along the critical manifold $\tilde{\mathcal{S}}_A$ is given by the reduced problem, Eq. (21). Substituting $\varphi(h)$ via Eq. (22) in Eq. (21a) yields:

$$\frac{d\sigma}{d\tau} \Big|_{(\sigma, h) \in \tilde{\mathcal{S}}_A} = \left(K_s - \frac{C\sigma}{\beta h} \right) \Big|_{\sigma=\varphi(h)} = \alpha K_h (h - h_*), \quad (25)$$

where h_* is given by Eq. (6); in Fig. 5(a), the fixed point $(K_s/\tilde{r}_0(h_*), h_*)$ of Eq. (21) is shown as a star. Using $d\sigma/d\tau = d\varphi(h)/d\tau = \varphi'(h) dh/d\tau$ and the derivative $\varphi'(h) = (\alpha K_h \beta / C)(1 - h/h_A)$, yields

$$\begin{aligned} \frac{dh}{d\tau} \Big|_{(\sigma, h) \in \tilde{\mathcal{S}}_A} &= \frac{d\sigma}{d\tau} \frac{1}{\varphi'(h)} \Big|_{(\sigma, h) \in \tilde{\mathcal{S}}_A} = \left(h - 1 + \frac{K_s}{\alpha K_h} \right) \frac{C/\beta}{1 - h/h_A} \\ &= -\frac{Ch_A(h - h_*)}{\beta(h - h_A)}, \end{aligned} \quad (26)$$

Both, $d\sigma/d\tau$ and $dh/d\tau$ flip sign at $h = h_*$. Restricting to $h > h_*$ and since $h_A > h_*$, the sign of the right-hand side of Eq. (26) is determined by the difference $h - h_A$ and changes at F_A . For $h > h_A$, the motion along the upper branch of the critical manifold occurs with $dh/d\tau < 0$ from smaller to larger values of σ , whereas $dh/d\tau > 0$ for motion on the lower branch, $h_* < h < h_A$, also see Fig. 5(a). These observations indicate that, in both cases, the motion along the attractive branch $\tilde{\mathcal{S}}_+$ and the repelling branch $\tilde{\mathcal{S}}_-$ for any $\sigma < \sigma_A$ is always towards the non-hyperbolic point F_A (in its vicinity).

Proposition 2. The critical manifold $\tilde{\mathcal{S}}_A$ possesses a single fold point, given by F_A in Eq. (23), and this point is a generic fold; in particular, it is nondegenerate and the flow at F_A is transversal to $\tilde{\mathcal{S}}_A$ (see Appendix B).

Proof. We have already observed that

$$\tilde{g}_0(F_A) = 0 \quad \text{and} \quad \partial_h \tilde{g}_0(F_A) = 0, \quad (27)$$

indicating that F_A is a fold point; it is also the only such point on $\tilde{\mathcal{S}}_A$, see Eq. (21b).

It remains to verify the nondegeneracy and transversality conditions on F_A . Indeed, we find from Eqs. (21) and (24) that

$$\partial_h^2 \tilde{g}_0(F_A) = -4K_h < 0, \quad \partial_\sigma \tilde{g}_0(F_A) = -\frac{2C}{\alpha\beta} < 0, \quad (28)$$

and

$$\tilde{f}_0(F_A) = \alpha K_h (h_A - h_*) > 0, \quad (29)$$

using $h_* > 0$ from Eq. (6). The conditions in Eq. (28) establish the nondegeneracy of the fold point. Together with the transversality condition, Eq. (29), this confirms that F_A is a generic fold point. \square

III.1.2. *Extension of slow manifolds through the fold point*

Recall that the stable branch $\tilde{\mathcal{S}}_+$ of the critical manifold is normally hyperbolic for all $h > h_A$. By the smoothness of the system, Fenichel's theorem guarantees that for any small $\gamma, \delta > 0$, the compact segment

$$\{(\varphi(h), h) : h \in [h_A + \gamma, 1 - \delta]\} \subset \tilde{\mathcal{S}}_+$$

gives rise to a nearby *slow manifold* $\tilde{\mathcal{S}}_{+,\varepsilon}$ for sufficiently small $\varepsilon > 0$, lying within an $\mathcal{O}(\varepsilon)$ -neighborhood of the critical manifold. Although uniqueness is not guaranteed, any such slow manifold can be written, up to first-order approximation, as the graph of a function $\varphi_\varepsilon(h) = \varphi(h) + \mathcal{O}(\varepsilon)$.

Standard GSPT ensures that any slow manifold can be extended beyond the fold point F_A , provided it is nondegenerate. Such an extension is illustrated in Fig. 5(b) for the dynamical system (16). Specifically, we consider the Poincaré sections

$$\tilde{\Sigma}_1 := \{(\sigma, h) : \sigma = \sigma_1, h \in \tilde{I}\}, \quad \tilde{\Sigma}_2 := \{(\sigma, h) : |\sigma - \sigma_A| \leq \delta, h = h_2\} \quad (30)$$

for some $0 < \sigma_1 < \sigma_A$, $0 < h_2 < h_A$, and an appropriate compact interval \tilde{I} , such that $\tilde{\mathcal{S}}_+ \cap \tilde{\Sigma}_1$ is not empty. The extension of $\tilde{\mathcal{S}}_{+,\varepsilon}$ beyond the fold point follows from the next proposition, which implies that, for any $\varepsilon > 0$ sufficiently small, also the intersection $\tilde{\mathcal{S}}_{+,\varepsilon} \cap \tilde{\Sigma}_1$ is nonempty and given by a point $(\sigma_1, \varphi(\sigma_1)) + \mathcal{O}(\varepsilon)$.

Transition map. Given two transversal sections $\tilde{\Sigma}_1$ and $\tilde{\Sigma}_2$, the *transition map* $\Pi_{1,2}^{(\varepsilon)} : \tilde{\Sigma}_1 \rightarrow \tilde{\Sigma}_2$ assigns to each point $(\sigma, h) \in \tilde{\Sigma}_1$ the first intersection point of the corresponding trajectory of the system (depending on ε) with $\tilde{\Sigma}_2$. That is, $\Pi_{1,2}^{(\varepsilon)}(\sigma, h)$ gives the location where the trajectory starting at (σ, h) reaches $\tilde{\Sigma}_2$. This map captures the evolution of trajectories between two phase space sections, which is central to understanding the global behavior of fast-slow systems.

Since F_A is a generic fold point (Prop. 2), the following statement is a direct consequence of Theorem 2.1 by Krupa and Szmolyan.⁴⁸ In particular, the transversality condition, Eq. (29), precludes the existence of a canard trajectory passing through F_A .

Proposition 3. For appropriate sections $\tilde{\Sigma}_1, \tilde{\Sigma}_2$ as defined above, the transition map $\Pi_{1,2}^{(\varepsilon)} : \tilde{\Sigma}_1 \rightarrow \tilde{\Sigma}_2$ is well-defined for sufficiently small $\varepsilon > 0$, and acts as an $\mathcal{O}(e^{-c_1/\varepsilon})$ -contraction for some $c_1 > 0$. Furthermore, for any $P \in \tilde{\Sigma}_1$, the image under the transition map satisfies

$$\Pi_{1,2}^{(\varepsilon)}(P) = \left(\sigma_A + \mathcal{O}(\varepsilon^{2/3}), h_2 \right). \quad (31)$$

III.2. The fold point F_B approached from the basic domain, at high pH

The candidate for a second fold point, later identified as F_B , corresponds to nearly neutral pH and is approached from the basic domain at $h \simeq \varepsilon C$ as $\varepsilon \rightarrow 0$ (cf. Eq. (44) below) and, in the limit, is pushed against the $h = 0$ axis (high pH level), hindering its analysis. To better resolve the properties of this point, we transform the dynamical system (8) by rescaling the h variable as

$$\eta := h/\varepsilon, \quad (32)$$

which effectively zooms into the vicinity of the $h = 0$ line. As a result, we arrive at the *fast-slow system*:

$$\frac{ds}{dt} = \hat{f}_\varepsilon(s, \eta) := -\hat{r}(\eta)s + K_s, \quad (33a)$$

$$\varepsilon \frac{d\eta}{dt} = \hat{g}_\varepsilon(s, \eta) := -\hat{q}_\varepsilon(s, \eta) + K_h(1 - \varepsilon\eta), \quad (33b)$$

with the rescaled functions $\hat{r}(\eta) := r_\varepsilon(\varepsilon\eta)$ and $\hat{q}_\varepsilon(s, \eta) := q_\varepsilon(s, \varepsilon\eta)$, see Eq. (9). Introducing the fast time $t' = t/\varepsilon$, the fast-slow system (33) takes the form:

$$\frac{ds}{dt'} = \varepsilon \hat{f}_\varepsilon(s, \eta), \quad (34a)$$

$$\frac{d\eta}{dt'} = \hat{g}_\varepsilon(s, \eta). \quad (34b)$$

For later use, we list the functions appearing on the r.h.s. of Eq. (33) for $\varepsilon = 0$:

$$\hat{r}(\eta) = \frac{1}{\beta C \eta^{-1} + 1 + (\beta/C)\eta}, \quad (35)$$

which does not depend on ε , and

$$\hat{q}_0(s, \eta) = \frac{1}{2} \sqrt{\hat{v}_0(\eta)^2 + 4AK\hat{r}(\eta)\eta^2 s} - \frac{\hat{v}_0(\eta)}{2}, \quad (36)$$

with

$$\hat{v}_0(\eta) := v_\varepsilon(\varepsilon\eta)|_{\varepsilon=0} = \alpha AK\eta^2 - K_h. \quad (37)$$

III.2.1. Critical manifold and singular dynamics

The corresponding *layer problem* is a one-dimensional dynamics in the fast variable η , parametrized by constant values of s . It is obtained by setting $\varepsilon = 0$ in (34):

$$\frac{ds}{dt'} = 0, \quad (38a)$$

$$\frac{d\eta}{dt'} = \hat{g}_0(s, \eta). \quad (38b)$$

The *reduced problem* follows by setting $\varepsilon = 0$ in (33) and reads:

$$\frac{ds}{dt} = \hat{f}_0(s, \eta) := -\hat{r}(\eta)s + K_s, \quad (39a)$$

$$0 = \hat{g}_0(s, \eta) := -\hat{q}_0(s, \eta) + K_h. \quad (39b)$$

The *critical manifold* is determined by the algebraic equation (39b):

$$\begin{aligned} \hat{\mathcal{M}}_B &:= \{(s, \eta) : \hat{g}_0(s, \eta) = 0\} \\ &= \{(s, \eta) : (\alpha K_h - \hat{r}(\eta)s)\eta^2 = 0\}; \end{aligned} \quad (40)$$

the second line follows from the equation $2\hat{q}_0(s, \eta) + \hat{v}_0(\eta) = 2K_h + \hat{v}_0(\eta)$ after substituting Eqs. (36) and (37) and taking the square. In particular, it is the union $\hat{\mathcal{M}}_B = \hat{\mathcal{S}}_B \cup \hat{\mathcal{L}}_B$ of a curve $\hat{\mathcal{S}}_B$ in the domain $\eta > 0$,

$$\hat{\mathcal{S}}_B = \{(\psi(\eta), \eta) : \eta > 0\} \quad \text{with} \quad \psi(\eta) := \frac{\alpha K_h}{\hat{r}(\eta)}, \quad (41)$$

and the s -axis, where $\eta = 0$:

$$\hat{\mathcal{L}}_B = \{(s, 0) : s \geq 0\}. \quad (42)$$

Inspection of the derivative

$$\psi'(\eta) = \alpha K_h (\beta/C) (1 - C^2/\eta^2) \quad (43)$$

shows that the branch $\hat{\mathcal{S}}_B$ has a unique fold point,

$$F_B := (s_B, \eta_B) = (\psi(\eta_B), \eta_B) = \left(\frac{\alpha K_h}{\hat{r}(\eta_B)}, C \right), \quad (44)$$

where one can further evaluate $\hat{r}(\eta_B) = 1/(2\beta + 1)$.

The stability of the critical manifold is inferred from the derivative of \hat{g}_0 along $\hat{\mathcal{S}}_B$. Using that \hat{g}_0 is constant on $\hat{\mathcal{S}}_B$, it holds

$$0 = d\hat{g}_0(s, \eta) = \partial_s \hat{g}_0(s, \eta) ds + \partial_\eta \hat{g}_0(s, \eta) d\eta; \quad (s, \eta) \in \hat{\mathcal{S}}_B. \quad (45)$$

Observing further that

$$\partial_s \hat{g}_0(s, \eta) = -\frac{AK\hat{r}(\eta)\eta^2}{2\hat{q}_0(s, \eta) + \hat{v}_0(\eta)}, \quad (46)$$

one readily computes

$$\begin{aligned} \partial_\eta \hat{g}_0(s, \eta) \Big|_{(s, \eta) \in \hat{\mathcal{S}}_B} &= -\partial_s \hat{g}_0(s, \eta) \psi'(\eta) \Big|_{(s, \eta) \in \hat{\mathcal{S}}_B} \\ &= \frac{(\beta/C)K_h \hat{r}(\eta)}{\eta^2 + K_h/(\alpha AK)} (\eta^2 - \eta_B^2), \end{aligned} \quad (47)$$

after inserting Eq. (43) and $\eta_B = C$.

Hence, the stability of the manifold $\hat{\mathcal{S}}_B$ depends on the sign of $\eta - \eta_B$: $\hat{\mathcal{S}}_B$ is stable for $\eta < \eta_B$ and unstable for $\eta > \eta_B$. Stated differently: $\hat{\mathcal{S}}_B$ is normally hyperbolic everywhere, except for the point F_B , where hyperbolicity is lost. Similarly to the manifold $\tilde{\mathcal{S}}_A$, with its fold point F_A , the manifold $\hat{\mathcal{S}}_B$ is divided at F_B into an attractive branch $\hat{\mathcal{S}}_+$, below F_B , and a repelling branch $\hat{\mathcal{S}}_-$, above F_B , which meet at the fold point, see Fig. 6(a).

The reduced flow on the critical manifold $\hat{\mathcal{S}}_B$ follows from Eq. (41) with Eq. (39a):

$$\left. \frac{ds}{dt} \right|_{(s, \eta) \in \hat{\mathcal{S}}_B} = (-\hat{r}(\eta)s + K_s) \Big|_{s=\psi(\eta)} = -\alpha K_h h_* < 0, \quad (48)$$

recalling h_* from Eq. (6). For the fast variable, we use $ds/dt = d\psi(\eta)/dt = \psi'(\eta) d\eta/dt$ and Eq. (43) to find:

$$\left. \frac{d\eta}{dt} \right|_{(s, \eta) \in \hat{\mathcal{S}}_B} = \frac{ds}{dt} \frac{1}{\psi'(\eta)} \Big|_{(s, \eta) \in \hat{\mathcal{S}}_B} = \frac{Ch_*}{\beta} \frac{\eta^2}{\eta_B^2 - \eta^2}. \quad (49)$$

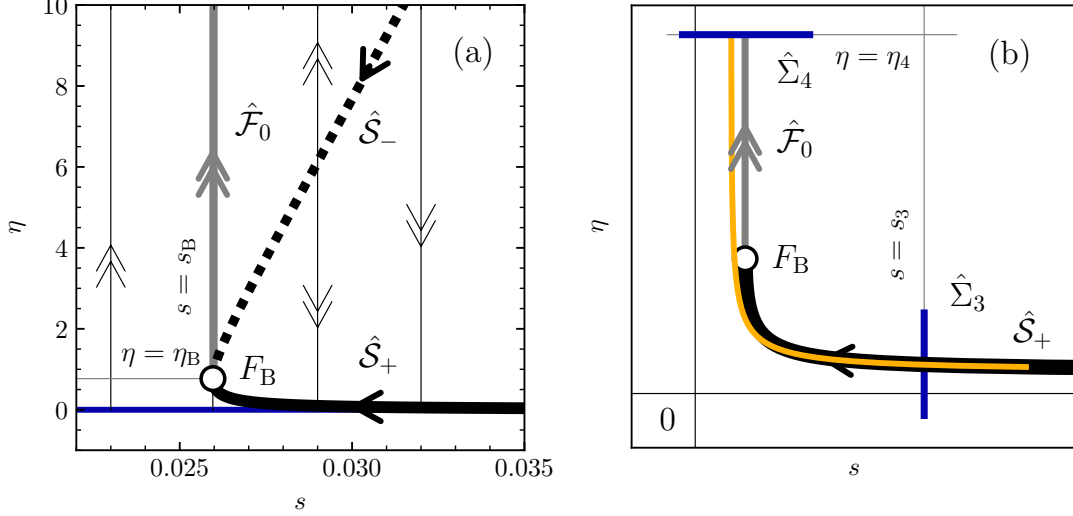


FIG. 6. (a) The nontrivial part $\hat{\mathcal{S}}_B = \hat{\mathcal{S}}_+ \cup \{F_B\} \cup \hat{\mathcal{S}}_-$ (thick black lines) of the critical manifold $\hat{\mathcal{M}}_B$ consists of the fold point F_B (circle, Eq. (44)), the attractive branch $\hat{\mathcal{S}}_+$ (solid line), and the repelling branch $\hat{\mathcal{S}}_-$ (dotted line), see Eq. (41). The trivial part $\hat{\mathcal{L}}_B$ of $\hat{\mathcal{M}}_B$ is the axis $\eta = 0$ (blue line). The slow motion along $\hat{\mathcal{S}}_+$ is governed by Eq. (49) and progresses left towards the generic fold point F_B , where a loss of hyperbolicity induces the switching to fast motion along the fast fiber. The segment of the fast fiber extending upwards from F_B , denoted as $\hat{\mathcal{F}}_0$ (thick gray line) is described by Eq. (38b) with $s = s_B$. The horizontal, thick green line marks $\eta = \eta_B$. (b) Schematic of the ε -perturbed extension (solid yellow line) of the critical manifold from panel (a), following $\hat{\mathcal{S}}_{+,\varepsilon}$ and passing near the fold point F_B . The Poincaré sections $\hat{\Sigma}_3$ and $\hat{\Sigma}_4$ are shown as dark blue lines; the thin gray lines are for $s = s_3$ and $\eta = \eta_4$, respectively; the remaining symbols are as in (a).

Since $C/\beta > 0$ and $h_* > 0$, the sign of $d\eta/dt$ on $\hat{\mathcal{S}}_B$ is equal to the sign of $\eta_B - \eta$. Starting a trajectory on the manifold at $\eta < \eta_B$, it evolves towards larger values of η and is accelerated upon approaching the singular point F_B , whereas the value of η decreases upon starting at $\eta > \eta_B$; in both cases, the value of s decreases with constant speed. In other words, the motion along the attractive branch $\hat{\mathcal{S}}_+$ and the repelling branch $\hat{\mathcal{S}}_-$ for any $s > s_B$ is always towards F_B , see Fig. 6(a). These observations are consistent with the following statement:

Proposition 4. The critical manifold $\tilde{\mathcal{S}}_B$ possesses a single fold point, given by F_B in Eq. (44), and this point is a generic fold.

Proof. We have already seen from Eq. (47) that $F_B \in \hat{\mathcal{S}}_B$ is a fold point, uniquely satisfying $\hat{g}_0(F_B) = 0$ and $\partial_\eta \hat{g}_0(F_B) = 0$. For the nondegeneracy of F_B , one verifies the stability along the fast direction,

$$\begin{aligned} \partial_\eta^2 \hat{g}_0(F_B) &= \frac{(\beta/C)K_h \hat{r}(\eta_B)}{\eta_B^2 + K_h/(\alpha AK)} \partial_\eta (\eta^2 - \eta_B^2) \Big|_{\eta=\eta_B} \\ &= 2\eta_B \frac{(\beta/C)K_h \hat{r}(\eta_B)}{\eta_B^2 + K_h/(\alpha AK)} > 0, \end{aligned} \quad (50)$$

and regularity along the slow direction,

$$\partial_s \hat{g}_0(F_B) = -\frac{\hat{r}(\eta_B)}{\alpha + K_h/(AK\eta_B^2)} < 0. \quad (51)$$

The first equation follows from Eq. (47), and we have used Eq. (46) with Eq. (37) to obtain the second relation. Finally, the transversality condition can be read off from Eq. (48):

$$\hat{f}_0(F_B) = -\alpha K_h h_* < 0. \quad (52)$$

Hence, F_B is a generic fold point. \square

III.2.2. Extension of slow manifolds through the fold point

Similarly to the situation of $\tilde{\mathcal{S}}_A$, any compact submanifold of $\hat{\mathcal{S}}_+$ persists for ε sufficiently small, and can be extended beyond F_B . Indeed, let

$$\hat{\Sigma}_3 := \{(s, \eta) : s = s_3, \eta \in \hat{I}\}, \quad \hat{\Sigma}_4 := \{(s, \eta) : |s - s_B| \leq \delta, \eta = \eta_4\} \quad (53)$$

for some $s_3 > s_B$, $\eta_4 > \eta_B$ and an appropriate compact interval \hat{I} ; see also Fig. 6(b). Analogously to Section III.1.2, the extension of any slow manifold $\hat{\mathcal{S}}_{+,\varepsilon}$ beyond the generic fold point F_B (Prop. 4) is given by the following statement, which is granted by Theorem 2.1 of Ref. 48. Again, a nonvanishing value of the flow in Eq. (52) excludes the possibility of canards at the point F_B .

Proposition 5. For appropriate sections $\hat{\Sigma}_3$ and $\hat{\Sigma}_4$ as defined in Eq. (53), the transition map $\Pi_{3,4}^{(\varepsilon)} : \hat{\Sigma}_3 \rightarrow \hat{\Sigma}_4$ is well-defined for sufficiently small $\varepsilon > 0$, and it acts as an $\mathcal{O}(e^{-c_2/\varepsilon})$ -contraction for some $c_2 > 0$. Furthermore, for any $P \in \hat{\Sigma}_3$, the image under the transition map satisfies

$$\Pi_{3,4}^{(\varepsilon)}(P) = (s_B, \eta_4) + \mathcal{O}(\varepsilon^{2/3}). \quad (54)$$

III.3. Global picture underlying the formation of the limit cycle

So far, we have clarified how two different scalings—essentially represented in Fig. 4 by the charts K_A and K_B , operating in different coordinates (σ, h) and (s, η) , respectively—resolve the dynamics around the fold points F_A and F_B . The existence of an attracting limit cycle was already established in Section II.2, and it now remains to connect these two perspectives to a global picture, revealing the formation and overall structure of the limit cycle. Our findings from the fast-slow analysis are then illustrated and corroborated by numerical solutions for limit cycle trajectories along the ε -perturbed slow manifolds and fast fibers.

III.3.1. Constructing the limit cycle from transition maps

Building on the results of Sections III.1 and III.2, we construct a sequence of Poincaré sections and their corresponding transition maps, as illustrated in Fig. 7:

$$\begin{aligned}
\Pi_{1,2}^{(\varepsilon)} : \tilde{\Sigma}_1 &\rightarrow \tilde{\Sigma}_2 \quad \text{for the passage of the fold point } F_A = (\sigma_A, h_A) \text{ in chart } K_A, \\
\Phi_{A,B} : \tilde{\Sigma}_2 &\rightarrow \hat{\Sigma}_2 \quad \text{for the transformation from chart } K_A \text{ to } K_B, \\
\Pi_{2,3}^{(\varepsilon)} : \hat{\Sigma}_2 &\rightarrow \hat{\Sigma}_3 \quad \text{for the transition towards the slow attracting manifold } \hat{\mathcal{S}}_+ \text{ in chart } K_B, \\
\Pi_{3,4}^{(\varepsilon)} : \hat{\Sigma}_3 &\rightarrow \hat{\Sigma}_4 \quad \text{for the passage of the fold point } F_B = (s_B, \eta_B) \text{ in chart } K_B, \\
\Phi_{B,A} : \hat{\Sigma}_4 &\rightarrow \tilde{\Sigma}_4 \quad \text{for the transformation from chart } K_B \text{ to } K_A, \\
\Pi_{4,1}^{(\varepsilon)} : \tilde{\Sigma}_4 &\rightarrow \tilde{\Sigma}_1 \quad \text{for the transition towards the slow attracting manifold } \tilde{\mathcal{S}}_+ \text{ in chart } K_A.
\end{aligned}$$

Here, $\hat{\Sigma}_2$ is the same as $\tilde{\Sigma}_2$ after a coordinate transformation from (σ, h) to (s, η) , and vice versa; $\tilde{\Sigma}_4$ is $\hat{\Sigma}_4$ in (σ, h) -coordinates. The individual steps are described in detail below. One full loop of the limit cycle is captured by the composition $\Pi : \tilde{\Sigma}_1 \rightarrow \tilde{\Sigma}_1$ of the above transition maps:

$$\Pi = \Pi_{1,2}^{(\varepsilon)} \circ \Phi_{A,B} \circ \Pi_{2,3}^{(\varepsilon)} \circ \Pi_{3,4}^{(\varepsilon)} \circ \Phi_{B,A} \circ \Pi_{4,1}^{(\varepsilon)}. \quad (55)$$

We note that working with an arbitrarily small, but nonzero $\varepsilon > 0$ is crucial for ensuring well-defined transformations between the charts K_A and K_B .

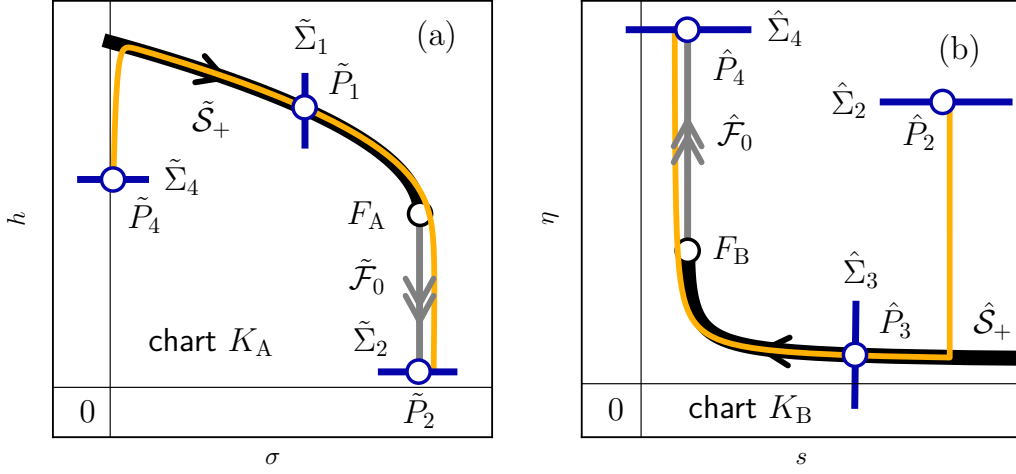


FIG. 7. Composition of the limit cycle from transition maps within and between the charts K_A and K_B , as described in Section III.3. The two panels depict the slow attractive manifolds $\tilde{\mathcal{S}}_+$, $\hat{\mathcal{S}}_+$ (solid black line), the fast fibers $\tilde{\mathcal{F}}_0$, $\hat{\mathcal{F}}_0$ (solid gray lines) in the singular limit, an ε -perturbed trajectory (solid yellow lines), and suitable Poincaré sections (dark blue lines). (a) Chart K_A uses coordinates (σ, h) to show the manifold $\tilde{\mathcal{S}}_+ \cup \tilde{\mathcal{F}}_0$, which determines the passage through the fold point F_A , and Poincaré sections $\tilde{\Sigma}_1$, $\tilde{\Sigma}_2$, $\tilde{\Sigma}_4$; with their intersection points $\tilde{P}_1 = \tilde{\Sigma}_1 \cap \tilde{\mathcal{S}}_+$, $\tilde{P}_2 = \tilde{\Sigma}_2 \cap \tilde{\mathcal{F}}_0$ and $\tilde{P}_4 = \tilde{\Sigma}_4 \cap \tilde{\mathcal{F}}_0 = \{\sigma = 0\}$. (b) Chart K_B uses coordinates (s, η) to show the manifold $\hat{\mathcal{S}}_+ \cup \hat{\mathcal{F}}_0$, which determines the passage through the fold point F_B , and Poincaré sections $\hat{\Sigma}_2$, $\hat{\Sigma}_3$, $\hat{\Sigma}_4$ with intersection points $\hat{P}_3 = \hat{\Sigma}_3 \cap \hat{\mathcal{S}}_+$ and $\hat{P}_4 = \hat{\Sigma}_4 \cap \hat{\mathcal{F}}_0$. The point \hat{P}_2 is identified with \tilde{P}_2 in chart K_A .

Description of $\Pi_{1,2}^{(\varepsilon)}$

The transition $\Pi_{1,2}^{(\varepsilon)}$ occurs within chart K_A and was characterized in Prop. 3. As detailed in Section III.1.1, the upper branch $\tilde{\mathcal{S}}_+$ of the slow critical manifold \mathcal{S}_A is quickly attracting. In the singular limit, $\varepsilon = 0$, the intersection of $\tilde{\Sigma}_1$ with $\tilde{\mathcal{S}}_+$, see Figure 5(b), is well-defined and corresponds to a certain point $\tilde{P}_1 := (\sigma_1, h_1) = (\varphi(h_1), h_1)$ for some $h_1 > 0$, with φ defined in Eq. (22). From \tilde{P}_1 , the trajectory follows the slow manifold $\tilde{\mathcal{S}}_+$ up to the fold point $F_A = (\sigma_A, h_A)$ (cf. Eq. (23)), as described in Section III.1.1, and then transitions to and along the fast fiber $\tilde{\mathcal{F}}_0$, Eq. (17b) with $\sigma = \sigma_A$. As a result, the trajectory follows the composite manifold $\tilde{\Gamma}_0 := \tilde{\mathcal{S}}_+ \cup \tilde{\mathcal{F}}_0$ and arrives at the point $\tilde{P}_2 := (\sigma_A, h_2) \in \tilde{\Sigma}_2$ for the Poincaré section $\tilde{\Sigma}_2$ defined in Eq. (30).

For the ε -perturbed case, the trajectory begins at a slightly shifted point, $\tilde{P}_{1,\varepsilon} \in \tilde{\Sigma}_1 \cap \tilde{\mathcal{S}}_{+,\varepsilon}$, follows the perturbed manifold $\tilde{\Gamma}_\varepsilon = \tilde{\mathcal{S}}_{+,\varepsilon} \cup \tilde{\mathcal{F}}_\varepsilon$, and reaches $\tilde{P}_{2,\varepsilon} := (\sigma_{A,\varepsilon}, h_2) \in \tilde{\Sigma}_2$. Both the fast fiber $\tilde{\mathcal{F}}_0$ and its perturbed continuation $\tilde{\mathcal{F}}_\varepsilon$ are transverse to $\tilde{\Sigma}_2$, ensuring that the transition map $\Pi_{1,2}^{(\varepsilon)}$ is well-defined.

Description of $\Phi_{A,B}$

The transformation $\Phi_{A,B} : \tilde{\Sigma}_2 \rightarrow \hat{\Sigma}_2$ facilitates the switch from the chart K_A with the coordinates (σ, h) to chart K_B with the coordinates (s, η) such that $\sigma = \varepsilon s$ and $\eta = h/\varepsilon$, see Eqs. (11) and (32). Hence, the Poincaré section $\tilde{\Sigma}_2$, as defined in chart K_A by Eq. (30), transforms into its counterpart in K_B :

$$\hat{\Sigma}_2 := \{(s, \eta) : |s - s_A| \leq \delta/\varepsilon, \eta = \eta_2\}, \quad (56)$$

where $s_A := \sigma_A/\varepsilon$ and $\eta_2 := h_2/\varepsilon$. For a small enough ε , this transformation is well-defined and unambiguous. As a result, the point $\tilde{P}_{2,\varepsilon} \in \tilde{\Sigma}_2$ in chart K_A corresponds to $\hat{P}_{2,\varepsilon} = (s_{A,\varepsilon}, \eta_2) := (\sigma_{A,\varepsilon}/\varepsilon, h_2/\varepsilon) \in \hat{\Sigma}_2$ in chart K_B .

Description of $\Pi_{2,3}^{(\varepsilon)}$

In chart K_B , the manifold $\hat{\mathcal{S}}_+$ and its perturbed counterpart $\hat{\mathcal{S}}_{+,\varepsilon}$ are strongly attractive, as obtained in Section III.2.1. Starting from the point $\hat{P}_{2,\varepsilon}$, the trajectory rapidly descends along the fast fiber at $s = s_{A,\varepsilon}$ until it approaches the manifold $\hat{\mathcal{S}}_{+,\varepsilon}$. Subsequently, it transitions to slow motion, drifting leftwards along $\hat{\mathcal{S}}_{+,\varepsilon}$, see Eq. (48), until it intersects the Poincaré section $\hat{\Sigma}_3$ at the point $\hat{P}_{3,\varepsilon} \in \hat{\Sigma}_3 \cap \hat{\mathcal{S}}_{+,\varepsilon}$.

Description of $\Pi_{3,4}^{(\varepsilon)}$

This transformation describes the passage through the fold point F_B , paralleling $\Pi_{1,2}^{(\varepsilon)}$; it occurs in chart K_B and was characterized in Prop. 5. The trajectory starts from the point $P_{3,\varepsilon} \in \hat{\Sigma}_3 \cap \hat{\mathcal{S}}_{+,\varepsilon}$ and follows the manifold $\hat{\Gamma}_\varepsilon = \hat{\mathcal{S}}_{+,\varepsilon} \cup \hat{\mathcal{F}}_\varepsilon$. Initially, the trajectory moves along the slow branch $\hat{\mathcal{S}}_{+,\varepsilon}$, passing through an ε -neighborhood of the fold point $F_B = (s_B, \eta_B)$, Eq. (44). Near the fold point, the trajectory transitions to the fast fiber $\hat{\mathcal{F}}_\varepsilon$, then rapidly moving upwards to reach the point $\hat{P}_{4,\varepsilon} := (s_{B,\varepsilon}, \eta_4) \in \hat{\Sigma}_4$ at the Poincaré section $\hat{\Sigma}_4$ in

Eq. (53). The fast fiber $\hat{\mathcal{F}}_0$ and its perturbed continuation $\hat{\mathcal{F}}_\varepsilon$ are transverse to $\hat{\Sigma}_4$, ensuring that the transition map $\Pi_{3,4}^{(\varepsilon)}$ is well-defined.

Description of $\Phi_{B,A}$

In analogy to $\Phi_{A,B}$, the transformation $\Phi_{B,A} : \hat{\Sigma}_4 \rightarrow \tilde{\Sigma}_4$ represents the switch from chart K_B back to chart K_A . Recalling the relation between the coordinates, $\sigma = \varepsilon s$ and $\eta = h/\varepsilon$, the Poincaré section $\hat{\Sigma}_4$ defined in chart K_B by Eq. (53) transforms in K_A into:

$$\tilde{\Sigma}_4 := \{(\sigma, h) : |\sigma - \sigma_B| \leq \varepsilon\delta, h = h_4\} , \quad (57)$$

where $\sigma_B := \varepsilon s_B$ and $h_4 := \varepsilon\eta_4$. For $\varepsilon > 0$, this transformation is well-defined and unambiguous. As a result, the point $\hat{P}_{4,\varepsilon} := (s_{B,\varepsilon}, \eta_4) \in \tilde{\Sigma}_4$ in chart K_B turns into the point $\tilde{P}_{4,\varepsilon} = (\sigma_{B,\varepsilon}, h_4) := (\varepsilon s_{B,\varepsilon}, \varepsilon\eta_4) \in \tilde{\Sigma}_4$ in chart K_A .

Description of $\Pi_{4,1}^{(\varepsilon)}$

In chart K_A , the manifold $\tilde{\mathcal{S}}_+$, and hence $\tilde{\mathcal{S}}_{+,\varepsilon}$, is strongly attractive, as we have found in Section III.2. This means that starting from the point $\tilde{P}_{4,\varepsilon}$, the trajectory rapidly ascends along the fast fiber with $\sigma = \sigma_{B,\varepsilon}$ until it approaches the manifold $\tilde{\mathcal{S}}_{+,\varepsilon}$. After that, the trajectory proceeds to slow motion, moving rightwards along $\tilde{\mathcal{S}}_{+,\varepsilon}$ until it reaches the Poincaré section $\tilde{\Sigma}_1$ at the initial point $\tilde{P}_{1,\varepsilon} \in \tilde{\Sigma}_1 \cap \tilde{\mathcal{S}}_{+,\varepsilon}$, which closes the orbit.

Overall, starting at the intersection point $\tilde{P}_{1,\varepsilon}$ of the slow attracting manifold $\tilde{\mathcal{S}}_{+,\varepsilon}$ with the Poincaré section $\tilde{\Sigma}_1$, we have demonstrated that the trajectory completes one full loop, ultimately returning to the same point $\tilde{P}_{1,\varepsilon}$.

III.3.2. Numerical results for the perturbed limit cycle

After having constructed the limit cycle for arbitrarily small $\varepsilon > 0$ as a perturbation of the critical manifold by means of GSPT, we test these predictions in Fig. 8 against a few representative limit cycle trajectories, interpolating between the real system and the idealised singular limit. The value $\varepsilon = 10^{-3}$ corresponds to the experimental system (1) and decreasing ε increases the degree of timescale separation. Trajectories were obtained for

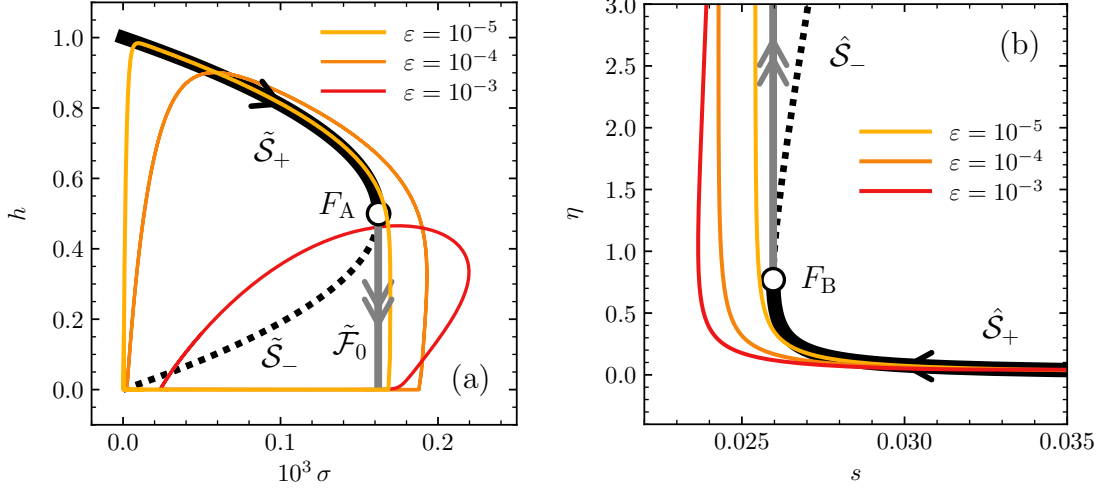


FIG. 8. Numerical solutions of Eq. (8) for ε -perturbed limit cycle trajectories for three values of ε (solid colored lines) in comparison to the critical manifold (black lines) and fast fibres (gray lines) of GSPT; all other parameters are the same as in Fig. 1 and Table III. The panels (a) and (b) correspond to the charts K_A and K_B in Fig. 7. (a) The full limit cycles in the coordinates (σ, h) , together with the fold point F_A , the critical manifold $\tilde{\mathcal{S}}_A = \tilde{\mathcal{S}}_+ \cup \tilde{\mathcal{S}}_-$ (black line, Eq. (22)), and the fast fiber $\tilde{\mathcal{F}}_0$ passing through F_A , cf. Section III.1. (b) The region near the fold point F_B using the coordinates (s, η) , showing parts of limit cycle trajectories (colored lines), the critical manifold $\hat{\mathcal{S}}_B = \hat{\mathcal{S}}_+ \cup \{F_B\} \cup \hat{\mathcal{S}}_-$ (black line, Eq. (41)), and the fast fiber through F_B (gray line), cf. Section III.2.

$\varepsilon = 1 \times 10^{-5}, 1 \times 10^{-4}, 1 \times 10^{-3}$ via numerical integration of Eq. (8) using Maple's `dsolve` routine with the stiff solver option and an absolute accuracy of 10^{-10} .

These numerical results neatly illustrate the emergence of fast-slow dynamics as ε decreases: the trajectories become increasingly aligned with the attractive branches of the slow critical manifold and the fast transition layers, as predicted by GSPT. In particular, the trajectory for $\varepsilon = 10^{-5}$ closely follows the ε -perturbed limit cycle, described in Section III.3 and Fig. 7. The sharp directional changes near the fold points F_A and F_B correspond well to the fast, jump-like motions along the associated fast fibers, while the trajectory segments in between trace the slow manifolds with high accuracy. The trajectory for $\varepsilon = 10^{-4}$ shows already pronounced deviations from the critical manifold and is intermediate between the real system ($\varepsilon = 10^{-3}$) and the idealized one ($\varepsilon = 10^{-5}$), highlighting the gradual approach to the critical manifold and the role of ε in controlling the degree of timescale separation.

The overall behavior of the numerical solutions not only corroborates the geometric picture established by the GSPT analysis, in Sections III.1 to III.3, but also demonstrates how the limit cycle converges to its singular limit in a piecewise manner – composed of alternating slow drifts and fast transitions.

IV. IMPLICATIONS FOR THE CHEMICAL SYSTEM

IV.1. Timescales and asymptotic estimates for the period

One of the central practical questions related to rhythms concerns the period of oscillations and how it depends on the parameters of the system. Our GSPT analysis of the limit cycle reveals trajectory segments evolving on distinct timescales, which enable estimation of the oscillation period. In particular, we find two distinct branches of slow dynamics, evolving through the acidic domain and the other through the basic domain, see Sections III.1 and III.2. These intervals of slow motion alternate with episodes of fast motion, forming a full cycle of oscillation, as shown in Section III.3. Under sufficient timescale separation, the contribution of the fast segments to the total period of oscillation becomes negligible, and the oscillation period is well approximated by the time spent along the slow branches. It should be noted that in the singular limit $\varepsilon = 0$, the period diverges and the limit cycle ceases to exist. However, for any arbitrarily small $\varepsilon > 0$, a limit cycle emerges and its period can be well approximated by the time required to traverse the corresponding branches of the critical manifold.

We now estimate the characteristic times $\mathcal{T}_{\text{acid}}$ and $\mathcal{T}_{\text{basic}}$ associated with the slow motion along the two branches of the limit cycle. The time $\mathcal{T}_{\text{acid}}$ corresponds to motion along the perturbed slow manifold $\tilde{\mathcal{S}}_{+,\varepsilon}$ in the acidic domain, approaching the ε -vicinity of the fold point F_A . Similarly, $\mathcal{T}_{\text{basic}}$ describes the slow return through the basic domain along $\hat{\mathcal{S}}_{+,\varepsilon}$ toward the neighborhood of the neutral fold point F_B . Notably, as is inferred from Fig. 1(d), the approach to F_B is distinctly slower than that to F_A . It is therefore of particular interest to understand the origin of this asymmetry in the dynamics.

Time spent in the acidic domain, along the branch $\tilde{\mathcal{S}}_+$ (chart K_A). Formally, the time $\mathcal{T}_{\text{acid}}$ for the motion along the acidic branch of the limit cycle is defined as

$$\mathcal{T}_{\text{acid}}(\varepsilon) := \int_{h_{\text{start}}}^{h_{\text{end}}} \left| \varepsilon \frac{dh_\varepsilon}{d\tau}(\sigma, h) \right|_{(\sigma, h) \in \tilde{\mathcal{S}}_{+, \varepsilon}}^{-1} dh, \quad (58)$$

where $dh_\varepsilon/d\tau$ is the ε -perturbed analog of reduced dynamics in Eq. (26) along the manifold $\tilde{\mathcal{S}}_{+, \varepsilon}$. The integration over h starts at h_{start} and ends at h_{end} , with the latter corresponding to the perturbed point $F_{A, \varepsilon} = F_A + O(\varepsilon^{2/3})$, see Prop. 3. In the similar way, the starting value of integration h_{start} is determined by the intersection of the fast fiber through $F_{B, \varepsilon}$ with the slow manifold $\tilde{\mathcal{S}}_{+, \varepsilon}$.

Aiming to obtain $\mathcal{T}_{\text{acid}}$ to leading order in ε , we approximate the perturbed manifold and fold points by their singular counterparts, which lie within an $O(\varepsilon^{2/3})$ vicinity, as suggested by Propositions 3 and 5. Accordingly, the derivative in Eq. (58) is approximated by $dh/d\tau$ from Eq. (26), evaluated along the stable branch $\tilde{\mathcal{S}}_+$ of the critical manifold $\tilde{\mathcal{S}}_A$. The upper limit of integration is taken to be $h_{\text{end}} \approx h_A = 1/2$, corresponding to the fold point F_A , see Eq. (23).

The critical manifold $\tilde{\mathcal{S}}_A$ is parametrized by the function $\varphi(h)$ given by Eq. (22), and the lower integration boundary h_{start} is determined by the condition $\varphi(h_{\text{start}}) \stackrel{!}{=} \sigma_B$, where $\sigma_B = \varepsilon s_B$ with $s_B = \alpha(2\beta + 1)K_h$ corresponding to the variable s taken at point F_B , see Eq. (44). This yields the quadratic equation $\alpha(\beta/C)K_h h_{\text{start}}(1 - h_{\text{start}}) \stackrel{!}{=} \varepsilon\alpha(2\beta + 1)K_h$ with respect to h_{start} . The larger root corresponds to the intersection with the stable part $\tilde{\mathcal{S}}_+$ of the critical manifold, and is given by $h_{\text{start}} = 1/2 + \sqrt{1/4 - \varepsilon C(2\beta + 1)/\beta}$, which simplifies to $h_{\text{start}} = 1 + \mathcal{O}(\varepsilon)$ for small ε .

With these ingredients, we obtain

$$\mathcal{T}_{\text{acid}}(\varepsilon) \approx \int_1^{h_A} \left| \varepsilon \frac{dh}{d\tau}(\sigma, h) \right|_{(\sigma, h) \in \tilde{\mathcal{S}}_+}^{-1} dh = -\frac{2\beta}{\varepsilon C} \int_1^{1/2} \frac{h - 1/2}{h - h_*} dh = \frac{\beta}{\varepsilon C} w(h_*) \quad (59)$$

with

$$w(h) = 1 - (1 - 2h) \ln \left(\frac{2 - 2h}{1 - 2h} \right). \quad (60)$$

Inserting $h_* \approx 0.0906$ from Eq. (6) into Eq. (59), we compute:

$$\mathcal{T}_{\text{up}}(\varepsilon) \approx 0.347 \frac{\beta}{\varepsilon C}. \quad (61)$$

Time spent in the basic domain, along the branch $\hat{\mathcal{S}}_+$ (chart K_B). As in the analysis of the acidic domain, we now evaluate the leading contribution to the oscillation period $\mathcal{T}_{\text{basic}}$ associated with motion along the branch of the limit cycle that lies in the basic domain. We approximate the perturbed manifold by the critical manifold $\hat{\mathcal{S}}_B$, whose stable branch $\hat{\mathcal{S}}_+$ is parametrized by the function $\psi(\eta)$, see Eq. (41). The time $\mathcal{T}_{\text{basic}}$ is obtained from Eq. (49) by integrating over η as $\mathcal{T}_{\text{basic}}(\varepsilon) \approx \int_{\eta_{\text{start}}}^{\eta_{\text{end}}} [(d\eta/dt)|_{\hat{\mathcal{S}}_+}]^{-1} d\eta$, where the integration limits η_{start} and η_{end} correspond to the intersections of the slow manifold $\hat{\mathcal{S}}_+$ with fast fibers passing through the fold points F_A and F_B , respectively; see Fig. 7.

The starting point η_{start} is defined by the condition $\psi(\eta_{\text{start}}) \stackrel{!}{=} s_A$, where $s_A = \sigma_A/\varepsilon$ (as in Eq. (56)) with $\sigma_A = \alpha\beta K_h/(4C)$ given by the fold point F_A , see Eq. (23). This leads to the quadratic equation $4\varepsilon\beta C\eta^2 - (\beta - 4\varepsilon C)\eta + 4\varepsilon\beta C^2 = 0$, whose smaller root corresponds to the intersection with the stable branch of the critical manifold $\hat{\mathcal{S}}_+$, yielding $\eta_{\text{start}} = [\beta - 4\varepsilon C - \sqrt{(\beta - 4\varepsilon C)^2 - (8\varepsilon\beta C)^2}]/(8\varepsilon\beta) = 4\varepsilon C^2 + \mathcal{O}(\varepsilon^2)$. Alternatively, this result follows by approximating $\psi(\eta) \simeq \alpha\beta K_h C/\eta$ in the limit $\eta \rightarrow 0$. The end point of integration is approximated by $\eta_{\text{end}} \approx \eta_B = C$, corresponding to the fold point F_B .

Combining these results, the time it takes to traverse the basic branch is evaluated to

$$\begin{aligned} \mathcal{T}_{\text{basic}}(\varepsilon) &\approx \int_{4\varepsilon C^2}^{\eta_B} \left(\frac{d\eta}{dt} \Big|_{\hat{\mathcal{S}}_+} \right)^{-1} d\eta = \frac{\beta}{Ch_*} \int_{4\varepsilon C^2}^{\eta_B} \frac{\eta_B^2 - \eta^2}{\eta^2} d\eta \\ &= -\frac{\beta}{h_*} \left(\frac{\eta}{C} + \frac{C}{\eta} \right) \Big|_{4\varepsilon C^2}^C = \frac{\beta}{h_*} \frac{(1 - 4\varepsilon C)^2}{4\varepsilon C} \approx \frac{\beta}{4\varepsilon Ch_*}. \end{aligned} \quad (62)$$

Inserting $h_* \approx 0.0906$ (Eq. (6)), we find

$$\mathcal{T}_{\text{basic}}(\varepsilon) \approx 2.76 \frac{\beta}{\varepsilon C}. \quad (63)$$

Thus, for the total oscillation period $\mathcal{T}(\varepsilon)$ to the leading order in ε , we obtain

$$\mathcal{T}(\varepsilon) \approx \mathcal{T}_{\text{acid}}(\varepsilon) + \mathcal{T}_{\text{basic}}(\varepsilon) = \frac{\beta}{\varepsilon C} \left(\frac{1}{4h_*} + w(h_*) \right) \approx 0.311 \frac{\beta}{\varepsilon C}. \quad (64)$$

In the last step, we substituted $h_* \approx 0.0906$. Note that a closer result with the prefactor 0.310 in the above expression follows if we approximate $w(h_*) \approx 1 - \ln(2) + \mathcal{O}(h_*)$ for small h_* .

We observe that both characteristic times, $\mathcal{T}_{\text{acid}}$ and $\mathcal{T}_{\text{basic}}$, are primarily governed by the same parameter combination, $\beta/(\varepsilon C)$. As a result, both timescales—and thus the total oscillation period—increase as ε decreases. This behavior is qualitatively consistent with

the fact that no limit cycle exists in the singular limit $\varepsilon = 0$: the motion along the reduced manifold then requires infinite time. Geometrically, this corresponds to the expansion of the limit cycle as $\varepsilon \rightarrow 0$, with its right boundary (which, in the singular limit, coincides with the acidic fold point, F_A) shifting toward larger values of s . This trend is also evident in Figs. 4(a) or 8(a), where one should recall that $\sigma = \varepsilon s$. Quantitatively, the scaling $\mathcal{T}_{\text{acid}}, \mathcal{T}_{\text{basic}} \sim \varepsilon^{-1}$ is consistent with other GSPT results, such as those obtained for the Brusselator model.⁴²

The ratio between the two timescales is independent of ε and given by

$$\frac{\mathcal{T}_{\text{acid}}(\varepsilon)}{\mathcal{T}_{\text{basic}}(\varepsilon)} \approx 4h_*w(h_*), \quad (65)$$

where $w(h_*)$ is given by Eq. (60). This expression confirms that the motion along the upper branch is considerably faster, provided $h_* \ll 1$. For $h_* \approx 0.0906$ (see details following Eq. (6)), and thus the GSPT prediction yields $\mathcal{T}_{\text{acid}}/\mathcal{T}_{\text{basic}} \approx 0.126$. It is important to note, however, that this asymmetry between timescales arises independently of the smallness of ε .

Timescales in physical units In dimensionless form, the durations $\mathcal{T}_{\text{acid}}$ and $\mathcal{T}_{\text{basic}}$ spent along the acidic and basic branches of the limit cycle are given by expressions Eqs. (59) and (62). To convert these to physical units, we use the rescaling relation $\varepsilon C = \varepsilon_1$ from Eq. (7) (see also Appendix A and Tables II and III). This yields the dimensional timescales:

$$T_{\text{acid}} = \frac{k_M}{v_{\text{max}}} \mathcal{T}_{\text{acid}} \approx \frac{k_M}{v_{\text{max}}} \frac{[\text{H}_{\text{ext}}^+]}{k_{\text{E1}}} w(h_*), \quad (66)$$

$$T_{\text{basic}} = \frac{k_M}{v_{\text{max}}} \mathcal{T}_{\text{basic}} \approx \frac{k_M}{v_{\text{max}}} \frac{[\text{H}_{\text{ext}}^+]}{k_{\text{E1}}} \frac{1}{4h_*}, \quad (67)$$

where k_M and v_{max} are the Michaelis–Menten constants, k_{E1} is the enzymatic rate constant at low pH, the function $w(h)$ is given by Eq. (60) and the fixed-point acid concentration of system Eq. (1) reads (cf. Eq. (6)):

$$h_* = \frac{[\text{H}_*^+]}{[\text{H}_{\text{ext}}^+]} = 1 - 2 \frac{k_S[\text{S}_{\text{ext}}]}{k_H[\text{H}_{\text{ext}}^+]}. \quad (68)$$

In the regime of strong timescale separation, the total oscillation period is generally approximated by the sum $T = T_{\text{acid}} + T_{\text{basic}}$, which is largely governed by the compound timescale $k_M[\text{H}_{\text{ext}}^+]/(v_{\text{max}}k_{\text{E1}})$. For small values of h_* , as in our case with $h_* \approx 0.0906$, we find $T_{\text{basic}}/T_{\text{acid}} = (4h_*w(h_*))^{-1} \approx 7.96$, see Eqs. (60) and (65). Thus, the oscillation period is dominated by the slow excursion along the basic branch, so that $T \approx T_{\text{basic}}$ as given in

Eq. (67); this observation is qualitatively consistent with the numerical data presented in Fig. 1(d). Generally, with the decrease in h_* , $T \approx T_{\text{basic}}$ grows as h_*^{-1} and if h_* approaches zero, where oscillations would disappear, the time spent on the lower branch diverges.

Comparison of analytic predictions with numerical data Finally, we compare the asymptotic analytic predictions obtained in the limit of strong timescale separation with numerical results from direct integration of Eq. (8) for $\varepsilon = 10^{-5}, 10^{-4}, 10^{-3}$, using the parameter values listed in Table III. The timescales spent along the slow branches in the acidic and basic domains, denoted by $\mathcal{T}_{\text{acid}}(\varepsilon)$ and $\mathcal{T}_{\text{basic}}(\varepsilon)$, are given analytically in Eqs. (59) and (62), respectively. As previously discussed, the total oscillation period excludes the fast transitions and is approximated by $\mathcal{T}(\varepsilon) \approx \mathcal{T}_{\text{acid}}(\varepsilon) + \mathcal{T}_{\text{basic}}(\varepsilon)$. From the numerical simulations, we estimate the corresponding timescales as the durations spent traveling from F_B to F_A and vice versa, denoted by $\tau_{B \rightarrow A}$ and $\tau_{A \rightarrow B}$, respectively. The full oscillation period is thus exactly $\tau = \tau_{B \rightarrow A} + \tau_{A \rightarrow B}$. The results, including the relative durations in each domain, are summarized in Table I. All timescales are presented in dimensionless units; physical times (in seconds) can be obtained by dividing by the rate constant $k_{\text{max}} \approx 6.17 \times 10^{-2} \text{ s}^{-1}$ (see Table II).

For smaller values of ε ($\varepsilon = 10^{-5}, 10^{-4}$), the numerical results agree reasonably well with the theoretical predictions, with closer agreement for $\varepsilon = 10^{-5}$ and slightly larger deviations at $\varepsilon = 10^{-4}$. In both cases, the numerically estimated timescales $\tau_{B \rightarrow A}$ and $\tau_{A \rightarrow B}$ slightly

ε	$\mathcal{T}_{\text{acid}}$	$\tau_{B \rightarrow A}$	$\mathcal{T}_{\text{basic}}$	$\tau_{A \rightarrow B}$	\mathcal{T}	τ	$\mathcal{T}_{\text{basic}}/\mathcal{T}_{\text{acid}}$	$\tau_{B \rightarrow A}/\tau_{A \rightarrow B}$
10^{-5}	900.95	975	7174.5	7.48×10^3	8075.5	8.46×10^3	7.9632	7.67
10^{-4}	90.095	120	717.45	825	807.55	945	7.9632	6.88
10^{-3}	9.0095	23.0	71.745	67.2	80.755	90.2	7.9632	2.92

TABLE I. Summary of the timescales obtained analytically and from numerical simulations for $\varepsilon = 10^{-5}, 10^{-4}, 10^{-3}$. The values of $\mathcal{T}_{\text{acid}}$ and $\mathcal{T}_{\text{basic}}$ are given by Eqs. (59) and (62) with $\mathcal{T} = \mathcal{T}_{\text{acid}} + \mathcal{T}_{\text{basic}}$. The data correspond to numerical solution of Eq. (8) and is identical to those in Fig. 8(a); all other parameters are the same as in Fig. 1 and Table III. The values of $\tau_{B \rightarrow A}$ and $\tau_{A \rightarrow B}$ corresponds to the time spent to move from points F_B to F_A and F_A to F_B , respectively, and $\tau = \tau_{B \rightarrow A} + \tau_{A \rightarrow B}$.

overestimate the analytic values $\mathcal{T}_{\text{acid}}$ and $\mathcal{T}_{\text{basic}}$, respectively. The deviations are smaller for the basic segment. This discrepancy is expected because the analytic estimates capture only the slow drift along the critical manifold, whereas the numerical values include both slow and fast phases of motion. Consistent with theory, the ratio of time spent in the basic domain to that in the acidic domain remains nearly independent of ε , with the theoretical value being approximately 8. From the numerical data, we find this ratio to be 7.7 for $\varepsilon = 10^{-5}$ and 6.9 for $\varepsilon = 10^{-4}$.

For $\varepsilon = 10^{-3}$, corresponding to the original system given by Eq. (1), the agreement between numerical and analytic values becomes less accurate. The time $\tau_{\text{B} \rightarrow \text{A}} \approx 23$ significantly overestimates the analytic value $\mathcal{T}_{\text{acid}} \approx 9$, while $\tau_{\text{A} \rightarrow \text{B}} \approx 67$ undershoots $\mathcal{T}_{\text{basic}} \approx 81$. As a result, the ratio $\tau_{\text{A} \rightarrow \text{B}}/\tau_{\text{B} \rightarrow \text{A}} \approx 3$ deviates substantially from the theoretical prediction $\mathcal{T}_{\text{basic}}/\mathcal{T}_{\text{acid}} \approx 8$. We attribute these larger discrepancies to the fact that the limit cycle for $\varepsilon = 10^{-3}$ deviates significantly from the singular cycle, as illustrated in Fig. 8.

IV.2. Differential transport across the membrane required for oscillations

Our study, including its geometric decomposition, not only provides a clear explanation for the existence and structure of the limit cycle but also uncovers additional insights into the conditions supporting oscillations. Among these, we identify a refined constraint for their emergence, expressed as $\alpha K_h > K_s$ (see Remark 1). In terms of the original parameters, this translates to

$$\frac{k_H}{k_S} > 2 \frac{[\text{S}_{\text{ext}}]}{[\text{H}_{\text{ext}}^+]}, \quad (69)$$

where k_H , k_S are transport rates across the membrane of the acid H^+ and substrate S, and $[\text{S}_{\text{ext}}]$, $[\text{H}_{\text{ext}}^+]$ are their external concentrations. Condition (69), which can be interpreted as a constraint on the differential transport, critical for sustained oscillatory behavior, sharpens requirements from prior studies,³⁸ such as $k_H/k_S > 1$, by explicitly linking transport rate asymmetry to external concentration ratios. Physically, this refined condition essentially imposes a condition on the relative strength of fluxes, namely: $k_H[\text{H}_{\text{ext}}^+] > 2k_S[\text{S}_{\text{ext}}]$.

For the stability diagram plotted in the coordinates $(k_H/k_S, [\text{S}_{\text{ext}}]/[\text{H}_{\text{ext}}^+])$ – as in Fig. 2 and in Fig. 6 of Ref. 39 – the condition in Eq. (69) defines the parameter domain above the line $k_H/k_S = 2[\text{S}_{\text{ext}}]/[\text{H}_{\text{ext}}^+]$ (which corresponds to $K_h/K_s = \alpha^{-1}$ in Fig. 2). This inequality thus

sets a lower bound for the domain of oscillations in the present reduced model, as oscillations can occur only in the parameter region above this line, where differential transport across the membrane is sufficiently strong. This analytical prediction aligns well with the numerically determined oscillatory domain reported in Ref. 39 (cf. their Fig. 6). Notably, the numerical data from that study further suggest that Eq. (69) must be satisfied together with the condition $[S_{\text{ext}}] \gtrsim [H_{\text{ext}}^+]$ to support sustained oscillations.

V. CONCLUSION

In this work, we have uncovered the geometric structure underlying the oscillatory dynamics of a biochemical pH oscillator, namely, the urea–urease reaction network confined to a lipid vesicle.^{24,26,38} Our analysis has built on a simple yet realistic model in two variables³⁹ and has used geometric singular perturbation theory (GSPT) as the central mathematical tool, providing us with a natural framework for resolving the fast–slow structure of the emerging limit cycle.

Despite the inherent presence of distinct fast and slow processes, the model lacks a single dominant small parameter that would directly control the timescale separation. Instead, it is controlled by several small dimensionless parameter combinations, none of which suffices to characterize the system’s multiscale behavior. We have overcome this challenge by a suitable formal coupling of such combinations, which enables the application of classical GSPT techniques.

Using this framework, we have identified distinct critical manifolds corresponding to the slow segments of the limit cycle—one in the acidic region, the other in the basic region. To resolve their local structures, we have introduced two separate rescalings, each tailored to the respective pH domain. This approach enables a detailed analysis of the system near the associated fold points, where normal hyperbolicity is lost. In particular, we have proven that these points are generic folds rather than canards, contrary to an earlier speculation.²⁵ A generalized GSPT, extended to handle degenerate equilibria,⁴⁸ has allowed us to rigorously track the dynamics through these non-hyperbolic regions. Finally, we have assembled a global picture of the oscillatory mechanism by matching the local analyses through suitably constructed transition maps.

One may also refrain from coupling the parameter combinations and work directly with

two small parameters ε_1 and ε_2 . This would induce the analysis of various regimes, where one of the parameters is small but fixed and the other is sent to 0. Note that this may uncover even more subtle substructures, as demonstrated for the peroxidase-oxidase reaction via a multiscale analysis of the Olsen model.⁴⁵ One could then also analyse a double-singular limit when $\varepsilon_1, \varepsilon_2 \rightarrow 0$, see also Ref. 51. For this work, we have focused on the main structure of the fast-slow limit cycle, yielding a first approximation within a simple coherent framework.

In parallel, there is a strong motivation to extend the present analysis of the deterministic dynamics to stochastic regimes. In biochemical systems, molecular fluctuations are inevitable and become increasingly pronounced as the system size decreases. Intrinsic noise, arising from the discreteness and finite copy numbers of molecules, is known to modify the dynamics of monostable enzymatic reaction networks,^{52,53} and can even lead to noise-induced oscillations.⁵⁴ In oscillatory systems, such noise effects can become especially pronounced near singularities such as fold points, where the system’s sensitivity to perturbations increases.⁵⁵ Indeed, an earlier numerical study by some of us²⁵ within the framework of the chemical master equation⁵⁶ demonstrated that periodic oscillations become increasingly irregular as noise intensifies, due to a decrease of vesicle size, eventually leading to a breakdown of rhythmicity. This suggests that the geometric structure identified through GSPT in the deterministic setting may continue to shape the dynamics as long as the noise is moderate. Supporting this idea, prior theoretical work has shown that slow manifolds persist in a probabilistic sense, and deviations due to noise can be quantified precisely.⁵⁷

ACKNOWLEDGMENTS

This research has been supported by the Deutsche Forschungsgemeinschaft (DFG) under Germany’s Excellence Strategy – MATH+: The Berlin Mathematics Research Center (EXC-2046/1) – Project No. 390685689 (Subproject AA1-18), in the case of M.E. also via Subprojects AA1-8 and EF45-5. Furthermore, M.E. thanks the DFG CRC 1114, the Einstein Foundation and the Dutch Research Council NWO (VI.Vidi.233.133) for support.

Appendix A: Connection with a realistic model of the urea–urease reaction

In the following, we relate the simplified model Eq. (1) and the model derived in Ref. 39, which is an already reduced, yet reliable model of the full urea–urease reaction network.³⁸

Let $[S]$ and $[H^+]$ denote the time-dependent concentrations substrate molecules (urea) and hydrogen ions within the vesicle and $[S_{\text{ext}}]$ and $[H_{\text{ext}}^+]$ refer to their constant values in the vesicle’s exterior, which acts as a reservoir. In terms of the dimensionless variables $s = [S]/[S_{\text{ext}}]$ and $h = [H^+]/[H_{\text{ext}}^+]$, the reaction kinetics of the urease-catalyzed hydrolysis of urea was shown to obey the dynamical system³⁹

$$\frac{ds}{dt} = -k_{\text{cat}}(s, h) s + k_S (1 - s), \quad (\text{A1a})$$

$$\frac{dh}{dt} = -k p(s, h) h + k_H (1 - h), \quad (\text{A1b})$$

for rate constants $k_S, k_H, k > 0$. The effective rate $k_{\text{cat}}(s, h) > 0$ expresses Michaelis–Menten kinetics with a pH-dependent reaction velocity and has the product form

$$k_{\text{cat}}(s, h) = k_{\text{cat}}^M(s[S_{\text{ext}}]) \cdot f_H(h[H_{\text{ext}}^+]) \quad (\text{A2})$$

with

$$k_{\text{cat}}^M([S]) = \frac{v_{\text{max}}}{k_M + [S]} \quad \text{and} \quad f_H([H^+]) = \frac{1}{1 + [H^+]/k_{E1} + k_{E2}/[H^+]}, \quad (\text{A3})$$

where v_{max} is the maximum reaction speed, k_M the Michaelis–Menten constant, and k_{E1} and k_{E2} are enzyme-specific H^+ concentrations. The bell-shaped function f_H attains its maximum at $[H^+]_{\text{max}} = (k_{E1}k_{E2})^{1/2}$ and its width scales as the ratio $\beta^{-2} := k_{E1}/k_{E2}$. The function $p(s, h) \geq 0$ appearing in Eq. (A1b) reads

$$p(s, h) = -\frac{b(h)}{2} + \frac{1}{2}\sqrt{b(h)^2 + 4c(s, h)} \quad (\text{A4})$$

with the abbreviations

$$b(h) := 1 + k'[H_{\text{ext}}^+]h + (1 - h^{-1}) k_H/k, \quad (\text{A5a})$$

$$c(s, h) := 2 k_{\text{cat}}(s, h)k'[S_{\text{ext}}]s/k \geq 0, \quad (\text{A5b})$$

and a constant $k' > 0$.

For the parameters of the model, Eqs. (A1)–(A5), we use the same values as in Ref. 39, which are listed in Table II. This choice of parameters introduces a timescale separation into

the model, which we exploit in this work to develop the GSPT analysis. Additionally, it allows for some *a priori* simplifications of the functional dependencies.

To obtain the simplified model of the main text, Eq. (1) together with Eqs. (2)–(4), we start by noting that Eqs. (A1a) and (A1b) imply bounded solutions $h(t), s(t) \in [0, 1]$. This follows from inspection of the signs of the r.h.s. of both equations and provided that the initial conditions satisfy these bounds. Moreover, the numerical solution for the limit cycle (Ref. 39 and Fig. 1) indicates that $s \lesssim 0.25$. Hence, there is a scale separation $s \ll k_M/[S_{\text{ext}}] \approx 7.9$ or, equivalently, for the substrate concentration, $[S] \ll k_M$. It allows us to approximately treat the Michaelis–Menten kinetics as a first-order (linear) reaction and to replace the catalytic rate by a constant, $k_{\text{cat}}^M([S]) \approx v_{\text{max}}/k_M =: k_{\text{max}}$. Additionally,

Parameter	Symbol	Value
external urea concentration	$[S_{\text{ext}}]$	$3.8 \times 10^{-4} \text{ M}$
external proton concentration	$[H_{\text{ext}}^+]$	$1.3 \times 10^{-4} \text{ M}$
maximum reaction speed	v_{max}	$1.85 \times 10^{-4} \text{ M s}^{-1}$
Michaelis-Menten constant	k_M	$3 \times 10^{-3} \text{ M}$
enzyme constant (low pH)	k_{E1}	$5 \times 10^{-6} \text{ M}$
enzyme constant (high pH)	k_{E2}	$2 \times 10^{-9} \text{ M}$
ammonia protonation rate	k_2	$4.3 \times 10^{10} \text{ M}^{-1} \text{ s}^{-1}$
ammonium deprotonation rate	k_{2r}	$2.4 \times 10^1 \text{ s}^{-1}$
proton transport rate	k_H	$9 \times 10^{-3} \text{ s}^{-1}$
urea transport rate	k_S	$1.4 \times 10^{-3} \text{ s}^{-1}$
ammonia outflow rate	k	$= k_S$
ammonium ion outflow rate	k_+	$= k_S$
$k_2/(k_{2r} + k_+) =$	k'	$1.79 \times 10^9 \text{ M}^{-1}$
$v_{\text{max}}/k_M =$	k_{max}	$6.17 \times 10^{-2} \text{ s}^{-1}$

TABLE II. Parameter values of the real-world chemical system for substance concentrations, enzyme properties, reaction rates, rates of differential transport across the vesicle membrane, and derived quantities.

$K_h =$	k_H/k_{\max}	0.15
$K_s =$	k_S/k_{\max}	0.023
$K =$	k/k_{\max}	0.023
$\alpha =$	$[H_{\text{ext}}^+]/(2[S_{\text{ext}}])$	0.17
$\beta =$	$\sqrt{k_{E2}/k_{E1}}$	0.02
$\varepsilon_1 =$	$\sqrt{k_{E1}k_{E2}}/[H_{\text{ext}}^+]$	7.7×10^{-4}
$\varepsilon_2 =$	$\alpha/(k'[H_{\text{ext}}^+])$	7.3×10^{-7}

TABLE III. Dimensionless parameter combinations of model (1).

the substrate concentration, over large parts of the limit cycle (cf. Fig. 1), is much smaller inside of the vesicle than in its exterior, $s \ll 1$ or $[S] \ll [S_{\text{ext}}]$, which suggests approximating the last term in Eq. (A1a) by a constant, $k_S(1-s) \approx k_S$, thereby simplifying the present analysis. Regarding the function $b(h)$, we note that $k'[H_{\text{ext}}^+] \approx 2.3 \times 10^5$ is a large constant and thus $1 + hk'[H_{\text{ext}}^+] \approx hk'[H_{\text{ext}}^+]$, except for tiny values of h , namely, for very low proton concentration $[H^+] \lesssim 1/k'$ in the basic regime, $\text{pH} \gtrsim 9.3$, which is not reached by the limit cycle (Fig. 1d).

In summary, provided that the solutions obey $0 \leq s \ll \min(k_M/[S_{\text{ext}}], 1)$ and $(k'[H_{\text{ext}}^+])^{-1} \ll h \leq 1$, Eq. (A1) can be replaced by

$$\frac{ds}{dt} = -k_{\max} f_H(h[H_{\text{ext}}^+]) s + k_S, \quad (\text{A6a})$$

$$\frac{dh}{dt} = -k p(s, h) h + k_H (1 - h). \quad (\text{A6b})$$

These equations coincide with the dynamical system Eq. (1) written in terms of the rescaled time $t' = k_{\max} t$ (and subsequently omitting the prime) and upon introducing dimensionless parameters $K_s := k_S/k_{\max}$, $K_h := k_H/k_{\max}$, and $K := k/k_{\max}$ and the functions given in Eqs. (2)–(4):

$$r(h) := f_H(h[H_{\text{ext}}^+]), \quad q(s, h) := K p(s, h) h, \quad \text{and} \quad v(h) := K b(h) h \quad (\text{A7})$$

with the parameters

$$\beta := \sqrt{k_{E2}/k_{E1}}, \quad \alpha := [H_{\text{ext}}^+]/(2[S_{\text{ext}}]), \quad (\text{A8a})$$

$$\varepsilon_1 := \sqrt{k_{E1}k_{E2}}/[H_{\text{ext}}^+], \quad \varepsilon_2 := 1/(2k'[S_{\text{ext}}]). \quad (\text{A8b})$$

We note that, in chemistry, one often uses logarithmic variables (pS, pH) instead of (s, h) , which are related to each other through

$$\text{pS} := -\log_{10}([S]/1 \text{ M}) = -\log_{10}(s) - \log_{10}([S_{\text{ext}}]/1 \text{ M}), \quad (\text{A9a})$$

$$\text{pH} := -\log_{10}([H^+]/1 \text{ M}) = -\log_{10}(h) - \log_{10}([H_{\text{ext}}^+]/1 \text{ M}). \quad (\text{A9b})$$

Table III lists the values of the above parameter combinations, for which the reduced and simplified system (1) exhibits a limit cycle, shown in Fig. 1. Previous work³⁹ and Fig. 2 show that the existence of a limit cycle sensitively depends on the ratio α of the external concentrations, which we keep fixed here. From Table III, one identifies ε_1 as a small parameter of the system; this ratio specifies by how much the external pH value deviates from the point, where the catalytic reaction velocity $\propto f_H$ attains its maximum, which is at $\text{pH} = 7$. Another small parameter is ε_2 , which is inversely proportional to the large parameter combination $k'[H_{\text{ext}}^+] = \alpha/\varepsilon_2$ mentioned above. The latter is the ratio between the H^+ concentration in the exterior of the vesicle and the effective equilibrium constant $1/k'$ of the $\text{NH}_3 + H^+ \rightleftharpoons \text{NH}_4^+$ conversion reaction, including the small outflow of NH_4^+ across the membrane. For the values given in Table III, one finds that ε_1^2 and ε_2 are of similar order of magnitude: $\varepsilon_1^2/\varepsilon_2 \approx 0.81$.

Appendix B: A primer on the analysis of fold points in GSPT

Here, we summarize the standard conditions that characterize *fold points* and distinguish *generic folds*.⁴⁰ Consider the slow time formulation of a fast–slow system,

$$\dot{x} = f(x, y), \quad \varepsilon \dot{y} = g(x, y) \quad (0 < \varepsilon \ll 1),$$

where x and y denote the slow and fast variables, respectively, and ε is a small parameter separating their timescales. A point $P := (x_0, y_0)$ on the critical manifold

$$\mathcal{C} := \{(x, y) : g(x, y) = 0\}$$

is called a *generic fold point* if the following conditions hold:

(i) *Fold point conditions:*

$$g(P) = 0, \quad \partial_y g(P) = 0,$$

which imply that P lies on the critical manifold \mathcal{C} and that the fast subsystem has a singularity at P . In particular, $\partial_y g(P) = 0$ corresponds to the loss of normal hyperbolicity of \mathcal{C} at P , since the linearization of the fast subsystem degenerates.

(ii) *Nondegeneracy conditions:*

$$\partial_y^2 g(P) \neq 0, \quad \partial_x g(P) \neq 0,$$

where $\partial_y^2 g(P) \neq 0$ ensures that the fold is quadratic (and therefore nondegenerate) in the fast variable, and $\partial_x g(P) \neq 0$ guarantees that the critical manifold varies regularly with the slow variable, preventing degeneracies also in the reduced (slow) flow.

(iii) *Transversality condition:*

$$f(P) \neq 0,$$

which ensures that the slow flow crosses the fold transversally, allowing trajectories to pass between attracting and repelling branches of the critical manifold. Together, conditions (i)–(iii) characterize P as a *generic fold point*, a structurally stable and nondegenerate singularity of the critical manifold where normal hyperbolicity is lost in a controlled manner. Away from fold points, where $\partial_y g \neq 0$, the critical manifold is normally hyperbolic.

If any of the conditions (i)–(iii) fails, the point P is a *nongeneric fold point*. In particular, if the transversality condition (iii) is violated so that $f(P) = 0$ then P is called a *folded singularity*. Such points represent a degeneracy where the slow flow is tangent to the fold, and this tangency is a necessary (though generally not sufficient) condition for the existence of *canard* solutions^{40,58,59}—special trajectories that follow both attracting and repelling branches of the critical manifold for significant time intervals.

REFERENCES

- ¹I. R. Epstein, “Nonlinear oscillations in chemical and biological systems,” [Physica D](#) **51**, 152–160 (1991).
- ²A. Goldbeter, *Biochemical Oscillations and Cellular Rhythms* (Cambridge University Press, Cambridge, 1996).

- ³I. R. Epstein and J. A. Pojman, *An Introduction to Nonlinear Chemical Dynamics: Oscillations, Waves, Patterns, and Chaos* (Oxford University Press, Oxford, 1998).
- ⁴B. Novák and J. J. Tyson, “Design principles of biochemical oscillators,” *Nat. Rev. Mol. Cell Biol.* **9**, 981–991 (2008).
- ⁵P. De Kepper, J. Boissonade, and I. Szalai, “From sustained oscillations to stationary reaction-diffusion patterns,” in *Chemomechanical Instabilities in Responsive Materials*, edited by P. Borckmans, P. De Kepper, A. R. Khokhlov, and S. Métens (Springer Netherlands, 2009) pp. 1–37.
- ⁶V. V. Yashin, O. Kuksenok, P. Dayal, and A. C. Balazs, “Mechano-chemical oscillations and waves in reactive gels,” *Rep. Progr. Phys.* **75**, 066601 (2012).
- ⁷N. Göth and J. Dzubiella, “Collective chemo-mechanical oscillations and cluster waves in communicating colloids,” *Commun. Phys.* **8**, 65 (2025).
- ⁸A. Goldbeter, “Oscillatory enzyme reactions and Michaelis–Menten kinetics,” *FEBS Letters* **587**, 2778–2784 (1993).
- ⁹N. Barkai and S. Leibler, “Robustness in simple biochemical networks,” *Nature (London)* **387**, 913–917 (1997).
- ¹⁰A. Cornish-Bowden, *Fundamentals of Enzyme Kinetics* (Portland Press, London, 2004).
- ¹¹U. Alon, *An Introduction to Systems Biology: Design Principles of Biological Circuits* (CRC Press, London, 2007).
- ¹²K. J. Rubin and P. Sollich, “Michaelis-Menten dynamics in protein subnetworks,” *J. Chem. Phys.* **144**, 174114 (2016).
- ¹³S. Milster, A. Darwish, N. Göth, and J. Dzubiella, “Synergistic chemomechanical dynamics of feedback-controlled microreactors,” *Phys. Rev. E* **108**, L042601 (2023).
- ¹⁴R. A. Alberty and V. Massey, “On the interpretation of the pH variation of the maximum initial velocity of an enzyme-catalyzed reaction,” *Biochim. Biophys. Acta* **13**, 347–353 (1954).
- ¹⁵M. Fidaleo and R. Lavecchia, “Kinetic study of enzymatic urea hydrolysis in the pH range 4–9,” *Chem. Biochem. Eng. Q.* **17**, 311–318 (2003).
- ¹⁶J. R. Casey, S. Grinstein, and J. Orlowski, “Sensors and regulators of intracellular pH,” *Nat. Rev. Mol. Cell Biol.* **11**, 50–61 (2010).
- ¹⁷G. Rábai, “Modeling and designing of pH-controlled bistability, oscillations and chaos in a continuous-flow stirred reactor,” *ACH – Models Chem.* 1998, 135, 381 **135**, 381–392

- (1998).
- ¹⁸R. McIlwaine, K. Kovacs, S. K. Scott, and A. F. Taylor, “A novel route to pH oscillators,” *Chem. Phys. Lett.* **417**, 39–42 (2006).
 - ¹⁹M. Orbán, K. Kurin-Csörgei, and I. R. Epstein, “pH-regulated chemical oscillators,” *Acc. Chem. Res.* **48**, 593–601 (2015).
 - ²⁰J. Horváth, I. Szalai, and P. De Kepper, “Designing stationary reaction–diffusion patterns in pH self-activated systems,” *Acc. Chem. Res.* **51**, 3183–3190 (2018).
 - ²¹B. Dúzs, I. Lagzi, and I. Szalai, “Functional rhythmic chemical systems governed by pH-driven kinetic feedback,” *ChemSystemsChem* **5**, e202200032 (2023).
 - ²²Y. Miele, T. Bánsági, A. F. Taylor, P. Stano, and F. Rossi, “Engineering enzyme-driven dynamic behaviour in lipid vesicles,” in *Advances in Artificial Life, Evolutionary Computation and Systems Chemistry*, edited by F. Rossi, F. Mavelli, P. Stano, and D. Caivano (Springer International Publishing, Cham, 2016) pp. 197–208.
 - ²³Y. Miele, T. Bánsági, A. F. Taylor, and F. Rossi, “Modelling approach to enzymatic pH oscillators in giant lipid vesicles,” in *Adv. Bionanomater.: Lecture Notes in Bioengineering*, edited by S. Piotto, F. Rossi, S. Concilio, E. Reverchon, and G. Cattaneo (Springer, Cham, 2018) pp. 63–74.
 - ²⁴F. Muzika, M. Růžicka, L. Schreiberová, and I. Schreiber, “Oscillations of pH in the urea–urease system in a membrane reactor,” *Phys. Chem. Chem. Phys.* **21**, 8619–8622 (2019).
 - ²⁵A. V. Straube, S. Winkelmann, C. Schütte, and F. Höfling, “Stochastic pH oscillations in a model of the urea–urease reaction confined to lipid vesicles,” *J. Phys. Chem. Lett.* **12**, 9888–9893 (2021).
 - ²⁶Y. Miele, S. J. Jones, F. Rossi, P. A. Beales, and A. F. Taylor, “Collective behavior of urease pH clocks in nano- and microvesicles controlled by fast ammonia transport,” *J. Phys. Chem. Lett.* **13**, 1979–1984 (2022).
 - ²⁷A. S. Leathard, P. A. Beales, and A. F. Taylor, “Design of oscillatory dynamics in numerical simulations of compartment-based enzyme systems,” *Chaos* **33**, 123128 (2023).
 - ²⁸D. Ridgway-Brown, A. S. Leathard, O. France, S. P. Muench, M. E. Webb, L. J. C. Jeuken, P. J. F. Henderson, A. F. Taylor, and P. A. Beales, “Membrane transport modulates the pH-regulated feedback of an enzyme reaction confined within lipid vesicles,” *ACS Nano* **19**, 9814–9825 (2025).

- ²⁹M. Itatani, G. Holló, P. Albanese, N. Valletti, S. Kurunczi, R. Horvath, F. Rossi, and I. Lagzi, “Temporal pH waveforms generated in an enzymatic reaction network in batch and cell-sized microcompartments,” [Cell Rep. Phys. Sci. **6**, 102367 \(2025\)](#).
- ³⁰G. Lente, G. Bazsa, and I. Fábián, “What is and what isn’t a clock reaction?” [New J. Chem. **31**, 1707–1707 \(2007\)](#).
- ³¹G. Hu, J. A. Pojman, S. K. Scott, M. M. Wrobel, and A. F. Taylor, “Base-catalyzed feedback in the urea-urease reaction,” [J. Phys. Chem. B **114**, 14059–14063 \(2010\)](#).
- ³²I. N. Bujanja, T. Bánsági, and A. F. Taylor, “Kinetics of the urea-urease clock reaction with urease immobilized in hydrogel beads,” [React. Kinet. Mech. Catal. **123**, 177–185 \(2018\)](#).
- ³³A. Q. Mai, T. Bánsági, A. F. Taylor, and J. A. Pojman, “A novel approach to cure-on-demand coatings using ammonia to catalyze thiol-acrylate and thiol-epoxy reactions,” [Commun. Chem. **4**, 101 \(2021\)](#).
- ³⁴C. Galanics and I. Szalai, “Dynamics of pH oscillators in continuous stirred tanks in series,” [ChemPhysChem **25**, e202400610 \(2024\)](#).
- ³⁵N. Bashir, A. S. Leathard, M. McHugh, I. Hoffman, F. Shaon, J. A. Belgodere, A. F. Taylor, and J. A. Pojman, “On the use of modelling antagonistic enzymes to aid in temporal programming of pH and pva–borate gelation,” [Mol. Syst. Des. Eng. **9**, 372–381 \(2024\)](#).
- ³⁶N. M. Ivanov, A. I. Slivkov, and W. T. S. Huck, “A urease-based pH photoswitch: A general route to light-to-pH transduction,” [Angew. Chem. Int. Ed. **64**, e202415614 \(2025\)](#).
- ³⁷M. A. A. Mahmud and J. A. Pojman, “A novel approach to cure-on-demand coatings using ammonia to catalyze thiol-acrylate and thiol-epoxy reactions,” [ACS Omega **10**, 20417–20426 \(2025\)](#).
- ³⁸T. Bánsági and A. F. Taylor, “Role of differential transport in an oscillatory enzyme reaction,” [J. Phys. Chem. B **118**, 6092–6097 \(2014\)](#).
- ³⁹A. V. Straube, S. Winkelmann, and F. Höfling, “Accurate reduced models for the pH oscillations in the urea–urease reaction confined to giant lipid vesicles,” [J. Phys. Chem. B **127**, 2955–2967 \(2023\)](#).
- ⁴⁰C. Kuehn, *Multiple Time Scale Dynamics*, Vol. 191 (Springer, 2015).
- ⁴¹M. Wechselberger, *Geometric Singular Perturbation Theory Beyond the Standard Form*, Vol. 6 (Springer, 2020).
- ⁴²M. Engel and G. Olicón Méndez, “A singular perturbation analysis for the Brusselator,”

- (2023), [arXiv:2311.00575 \[math.DS\]](#).
- ⁴³I. Gucwa and P. Szmolyan, “Geometric singular perturbation analysis of an autocatalator model,” [Discrete Contin. Dyn. Syst. Ser. S](#) **2**, 783–806 (2009).
- ⁴⁴I. Kosiuk and P. Szmolyan, “Scaling in singular perturbation problems: blowing up a relaxation oscillator,” [SIAM J. Appl. Dyn. Syst.](#) **10**, 1307–1343 (2011).
- ⁴⁵C. Kuehn and P. Szmolyan, “Multiscale geometry of the Olsen model and non-classical relaxation oscillations,” [J. Nonlinear Sci.](#) **25**, 583–629 (2015).
- ⁴⁶M. Acar, D. Tatini, V. Romani, B. W. Ninham, F. Rossi, and P. Lo Nostro, “Curious effects of overlooked aspects on urease activity,” [Colloids Surf. B Biointerfaces](#) **247**, 114422 (2025).
- ⁴⁷N. Fenichel, “Geometric singular perturbation theory for ordinary differential equations,” [J. Diff. Equat.](#) **31**, 53–98 (1979).
- ⁴⁸M. Krupa and P. Szmolyan, “Extending geometric singular perturbation theory to non-hyperbolic points – fold and canard points in two dimensions,” [SIAM J. Math. Anal.](#) **33**, 286–314 (2001).
- ⁴⁹Y. A. Kuznetsov, [Elements of Applied Bifurcation Theory](#), 3rd ed., Applied Mathematical Sciences, Vol. 112 (Springer, New York, 2004).
- ⁵⁰E. A. Coddington and N. Levinson, [Theory of ordinary differential equations](#) (McGraw-Hill Book Co., Inc., New York-Toronto-London, 1955) pp. xii+429.
- ⁵¹C. Kuehn, N. Berglund, C. Bick, M. Engel, T. Hurth, A. Iuorio, and C. Soresina, “A general view on double limits in differential equations,” [Phys. D](#) **431**, Paper No. 133105, 26 (2022).
- ⁵²P. Thomas, A. V. Straube, and R. Grima, “Stochastic theory of large-scale enzyme-reaction networks: Finite copy number corrections to rate equation models,” [J. Chem. Phys.](#) **133**, 195101 (2010).
- ⁵³P. Thomas, A. V. Straube, and R. Grima, “The slow-scale linear noise approximation: An accurate, reduced stochastic description of biochemical networks under timescale separation conditions,” [BMC Syst. Biol.](#) **6**, 39 (2012).
- ⁵⁴P. Thomas, A. V. Straube, J. Timmer, C. Fleck, and R. Grima, “Signatures of nonlinearity in single cell noise-induced oscillations,” [J. Theor. Biol.](#) **335**, 222–234 (2013).
- ⁵⁵M. Engel and G. Olicón-Méndez, “Noise-induced instabilities in a stochastic Brusselator,” in [Topics in multiple time scale dynamics](#), Contemp. Math., Vol. 806 (Amer. Math. Soc., [Providence], RI, [2024] ©2024) pp. 29–47.

- ⁵⁶S. Winkelmann and C. Schütte, *Stochastic Dynamics in Computational Biology*, Vol. 645 (Springer, 2020).
- ⁵⁷N. Berglund and B. Gentz, *Noise-Induced phenomena in Slow-Fast Dynamical Systems: A Sample-Paths Approach*, Probability and Its Applications (Springer, 2006).
- ⁵⁸E. Benoît, J. F. Callot, F. Diener, and M. Diener, “Chasse au canard,” [Collectanea Mathematica](#) **31-32**, 37–119 (1997).
- ⁵⁹M. Krupa and P. Szmolyan, “Relaxation oscillation and canard explosion,” [J. Diff. Equat.](#) **174**, 312–368 (2001).